Monthly Notices of the ROYAL ASTRONOMICAL SOCIETY

MNRAS **500,** 5056–5071 (2021) doi:10.1093/mnras/staa3523
Advance Access publication 2020 November 12

Cosmology dependence of halo masses and concentrations in hydrodynamic simulations

Antonio Ragagnin,[1,2]★ Alexandro Saro,[3,2,1,4] Priyanka Singh[1,2] and Klaus Dolag[5,6]

[1]*INAF – Osservatorio Astronomico di Trieste, via G.B. Tiepolo 11, I-34143 Trieste, Italy*
[2]*IFPU – Institute for Fundamental Physics of the Universe, Via Beirut 2, I-34014 Trieste, Italy*
[3]*Astronomy Unit, Department of Physics, University of Trieste, via Tiepolo 11, I-34131 Trieste, Italy*
[4]*INFN - National Institute for Nuclear Physics, Via Valerio 2, I-34127 Trieste, Italy*
[5]*Fakultät für Physik, Universitäts-Sternwarte München, LMU Munich, Scheinerstr 1, D-81679 München, Germany*
[6]*Max-Planck-Institut für Astrophysik (MPA), Karl-Schwarzschild Strasse 1, D-85748 Garching bei München, Germany*

Accepted 2020 November 9. Received 2020 November 6; in original form 2020 March 5

ABSTRACT

We employ a set of Magneticum cosmological hydrodynamic simulations that span over 15 different cosmologies, and extract masses and concentrations of all well-resolved haloes between $z = 0$ and 1 for critical overdensities $\Delta_{\rm vir}$, Δ_{200c}, Δ_{500c}, Δ_{2500c} and mean overdensity Δ_{200m}. We provide the first mass–concentration (Mc) relation and sparsity relation (i.e. $M_{\Delta 1} - M_{\Delta 2}$ mass conversion) of hydrodynamic simulations that is modelled by mass, redshift, and cosmological parameters $\Omega_{\rm m}$, $\Omega_{\rm b}$, σ_8, h_0 as a tool for observational studies. We also quantify the impact that the Mc relation scatter and the assumption of Navarro–Frank–White (NFW) density profiles have on the uncertainty of the sparsity relation. We find that converting masses with the aid of an Mc relation carries an additional fractional scatter (≈ 4 per cent) originated from deviations from the assumed NFW density profile. For this reason, we provide a direct mass–mass conversion relation fit that depends on redshift and cosmological parameters. We release the package HYDRO_MC, a PYTHON tool that perform all kind of conversions presented in this paper.

Key words: Galaxy: halo – cosmological parameters – large-scale structure of Universe.

1 INTRODUCTION

Early studies of numerical *N*-body simulations of cosmic structures embedded in cosmological volumes (see e.g. Kravtsov, Klypin & Khokhlov 1997; Navarro, Frenk & White 1997) showed that dark matter haloes can be described by the so-called Navarro–Frank–White (NFW) profile (Navarro, Frenk & White 1996). The NFW density profile $\rho(r)$ is modelled by a characteristic density ρ_0 and a scale radius $r_{\rm s}$ in the following way:

$$\rho\left(r\right) = \frac{\rho_0}{\frac{r}{r_{\rm s}}\left(1+\frac{r}{r_{\rm s}}\right)^2}. \tag{1}$$

The NFW profile proved to match density profiles of dark matter haloes of dark matter-only (DMO) simulations (see e.g. Bullock et al. 2001; Suto 2003; Prada et al. 2012; Meneghetti et al. 2014; Klypin et al. 2016; Gupta et al. 2017; Brainerd 2019) up to the largest and most resolved ones whose analyses trace the route for the next generation of (pre-)Exascale simulations. However, density profiles of hydrodynamic simulations have small deviations from the NFW profile (see e.g. Balmès et al. 2014; Tollet et al. 2016).

Since this kind of density profile does not have a cut-off radius, the radius of a halo is often chosen as the virial radius $R_{\rm vir}$ (see e.g. Ghigna et al. 1998; Frenk et al. 1999), namely the radius at which the mean density crosses the one of a theoretical virialized homogeneous top-hat overdensity. Bryan & Norman (1998) showed that the virial overdensity can be written as

$$\Delta_{\rm vir}(a) \approx 18\pi^2 + 82\Omega\left(a\right) - 39\Omega\left(a\right), \tag{2}$$

where a is the scale factor and $\Omega(a)$ is the energy density parameter (see Dodelson 2003, for a review), namely

$$\Omega(a) = \Omega_{\rm m}a^3 \times \left(\frac{\Omega_{\rm m}}{a^3} + \frac{\Omega_{\rm r}}{a^4} + \frac{\Omega_{\rm k}}{a^2} + \Omega_\Lambda\right)^{-1}, \tag{3}$$

where $\Omega_{\rm m}$, $\Omega_{\rm r}$, $\Omega_{\rm k}$, and Ω_Λ are the density fractions of the total matter, radiation, curvature, and cosmological constant, respectively. Numerical cosmological simulations, as in this work, typically use negligible radiation and curvature terms (they set $\Omega_{\rm r} = \Omega_{\rm k} = 0$ in equation 3).

Observational studies typically define galaxy cluster (GC) radii as $R_{\Delta c}$, where Δ is an arbitrary overdensity and the 'c' suffix indicates that the overdensity is relative to the critical overdensity given by

$$M(r < R_{\Delta c}) = \Delta \times \frac{4}{3}\pi R_{\Delta c}^3 \rho_{\rm c}. \tag{4}$$

X-ray observations typically use overdensities Δ_{500c} and Δ_{2500c} and the corresponding radii R_{500c} and R_{2500c} (see e.g. Bocquet et al. 2019; Bulbul et al. 2019; Mantz 2019; Umetsu et al. 2019), whereas observational studies that compute dynamical masses typically use $\Delta = \Delta_{200c}$ (see e.g. Biviano et al. 2017; Capasso et al. 2019). Weak-lensing studies on the other hand often utilize radii whose overdensities are proportional to the mean density of the Universe. For instance, works such as Mandelbaum, Seljak & Hirata (2008) and McClintock et al. (2019) measure halo radii

★ E-mail: antonio.ragagnin@inaf.it

as R_{200m}, where the suffix 'm' means that the radius is defined so the mean density of the halo in equation (4) crosses $\Delta\overline{\rho}$ (in this case $200\overline{\rho}$), where $\overline{\rho}$ is the average matter density of the Universe.

The concentration c_Δ of a halo is defined as $c_\Delta \equiv R_\Delta/r_s$, where r_s is the scale radius of equation (1) and quantifies how large the internal region of the cluster is compared to its radius for a given overdensity (see Okoli 2017, for a review). Both numerical and observational studies analyse the concentration of haloes in the context of the so-called mass–concentration (Mc) plane (see table 4 in Ragagnin et al. 2019, for comprehensive list of recent studies). Within the context of hydrodynamic simulations, one can define the DM Mc plane that can be used by observations that estimate DM profiles (e.g. Merten et al. 2015). On the other hand, observations that have only information on the total matter profile must rely on total matter Mc planes (e.g. Raghunathan et al. 2019).

In search of a realistic estimate of halo concentrations, one must consider the various sources that affect this value. The c parameter in both observational and numerical studies is found to have a weak dependence on halo mass and a very large scatter (Bullock et al. 2001; Martinsson et al. 2013; Ludlow et al. 2014; Shan et al. 2017; Shirasaki, Lau & Nagai 2018; Ragagnin et al. 2019). Concentration has been found to depend on a number of factors, as formation time of haloes (Bullock et al. 2001; Rey, Pontzen & Saintonge 2018), accretion histories (see e.g. Ludlow et al. 2013; Fujita et al. 2018a, b), dynamical state (Ludlow et al. 2012), triaxiality (Giocoli et al. 2012, 2014), and halo environment (Klypin et al. 2016; Corsini et al. 2018). The fractional scatter in the Mc plane is larger than $\gtrsim 33$ per cent (Heitmann et al. 2016), and observations found outliers both with an extremely high concentration (Buote & Barth 2019) or very low concentration. When all major physical phenomena of galaxy formation are taken into account (cooling, star formation, black hole seeding and their feedback), then concentration parameters are lower than their DMO counterpart (see e.g. results from NIHAO simulations as in Wang et al. 2015; Tollet et al. 2016).

Halo concentration parameters are also affected by the underlying cosmological model (see e.g. Roos 2003, for a review on cosmological models). The derived Mc relation is found in fact different in cold dark matter (CDM), ΛCDM, wDM, and varying dark energy equation of state (Kravtsov et al. 1997; Dolag et al. 2004; De Boni 2013; De Boni et al. 2013; Ludlow et al. 2016). In general, the Mc dependence of DMO simulations on cosmological parameters has been extensively studied in works such as the Cosmic Emulator (Macciò, Dutton & van den Bosch 2008; Bhattacharya et al. 2013; Heitmann et al. 2016), Ludlow et al. (2014), and Prada et al. (2012).

Mc relations allow observational works to convert masses between overdensities. For this purpose, Balmès et al. (2014) defined the sparsity parameter $s_{\Delta 1,\,\Delta 2}$ as the ratio between masses at overdensity Δ_1 and Δ_2. This quantity is a proxy to the total matter profile (Corasaniti et al. 2018) and enables cosmological parameter inference (Corasaniti & Rasera 2019) and testing for some dark energy models without assuming an NFW profile (Balmès et al. 2014). Observations use the sparsity parameter to infer the halo matter profile (Bartalucci et al. 2019), as a potential probe to test $f(R)$ models (Achitouv et al. 2016), a less uncertain measurement of the Mc relation (Fujita et al. 2019), and to find outliers in scaling relations involving integrated quantities with different radial dependences (see conclusions in Andreon et al. 2019).

In this work, we use data from the Magneticum suite of simulations (presented in works such as Biffi, Dolag & Böhringer 2013; Saro et al. 2014; Dolag et al. 2015; Steinborn et al. 2015; Teklu et al. 2015; Bocquet et al. 2016; Dolag, Komatsu & Sunyaev 2016; Steinborn et al. 2016; Remus et al. 2017) to calibrate the cosmology dependence of the Mc and of the mass–sparsity relation of the total matter component from hydrodynamic simulations with the purpose of facilitating cluster–cosmology oriented studies. These studies typically calibrate the observable–mass relation from stacked weak-lensing signal under the assumption that mass calibration can be correctly recovered from DMO Mc relations (e.g. Dietrich et al. 2014; Rozo et al. 2014; Baxter et al. 2016; Geach & Peacock 2017; Simet et al. 2017; McClintock et al. 2019; Raghunathan et al. 2019 and references therein), an approximation that has to be quantified by calibrating the total mass Mc relations within hydrodynamic simulations (see discussion in section 5.4.1 of McClintock et al. 2019).

This work represents a first necessary step in this direction and it provides Mc and mass–mass relations that depend on cosmology and that simultaneously account for the presence of baryons. While in fact previous works in the literature studied either the dependence of the concentration on cosmological parameters or on baryon physics, in this analysis we calibrate for the first time the dependence of concentration on cosmological parameters in the context of hydrodynamic simulations that include a full description of the main baryonic physical processes.

In Section 2, we present the numerical set-up of the simulations used in this work. In Section 3, we fit the concentration of haloes as a function of mass and scale factor for all our simulations and compare our results with both observations and other theoretical studies. In Section 4, we provide a fit of the concentration as a function of mass, scale factor, and cosmology. As uncertainty propagation is a delicate and important matter for cluster cosmology experiments, in Section 5 we test sparsity parameter and study the origin of its large uncertainty. In order to facilitate cluster cosmology studies that include mass–observable relations that are calibrated at different radii (e.g. Bocquet et al. 2016, 2019; Costanzi et al. 2019; Mantz 2019), we study how to convert masses at different overdensities (the sparsity–mass relation). We summarize our findings, including a careful characterization of the associated intrinsic scatter in Section 5. We draw our conclusions in Section 7.

2 NUMERICAL SIMULATIONS

Magneticum simulations are performed with an extended version of the N-body/smoothed particle hydrodynamics (SPH) code P-GADGET3, which is the successor of the code P-GADGET2 (Springel 2005; Springel et al. 2005b; Boylan-Kolchin et al. 2009), with a space-filling curve aware neighbour search (Ragagnin et al. 2016), an improved SPH solver (Beck et al. 2016); treatment of radiative cooling, heating, ultraviolet (UV) background, star formation, and stellar feedback processes as in Springel, Di Matteo & Hernquist (2005a), connected to a detailed chemical evolution and enrichment model as in Tornatore et al. (2007), which follows 11 chemical elements (H, He, C, N, O, Ne, Mg, Si, S, Ca, and Fe) with the aid of CLOUDY photoionization code (Ferland et al. 1998). Fabjan et al. (2010) and Hirschmann et al. (2014) describe prescriptions for black hole growth and for feedback from active galactic nuclei (AGNs).

Haloes are identified using the version of SUBFIND (Springel et al. 2001), adapted by Dolag et al. (2009) to take the baryon component into account.

Table 1. List of Magneticum simulations as presented in Singh et al. (2019). Columns show, respectively: simulation name, cosmological parameters Ω_m, Ω_b, σ_8, and h_0, the number of haloes selected from all redshift snapshots ($z = 0.00,\ 0.14,\ 0.29,\ 0.47,\ 0.67$, and $z = 0.9$) of a given simulation, and the number of haloes of that simulations at redshift $z = 0$. Two of these simulations were also run without radiative processes (C1_norad and C1_norad) and C8 uses the reference cosmology from Komatsu et al. (2011).

Name	Ω_m	Ω_b	σ_8	h_0	N_{haloes} (All snapshots)	N_{haloes} (Snapshot $z = 0$)
C1	0.153	0.0408	0.614	0.666	29 206	9153
C1_norad	0.153	0.0408	0.614	0.666	27 613	9208
C2	0.189	0.0455	0.697	0.703	54 094	16 236
C3	0.200	0.0415	0.850	0.730	107 423	27 225
C4	0.204	0.0437	0.739	0.689	66 351	19 051
C5	0.222	0.0421	0.793	0.676	84 087	22 037
C6	0.232	0.0413	0.687	0.670	47 045	14 930
C7	0.268	0.0449	0.721	0.699	58 815	17 990
C8	0.272	0.0456	0.809	0.704	79 417	22 353
C9	0.301	0.0460	0.824	0.707	96 151	26 473
C10	0.304	0.0504	0.886	0.740	120 617	32 551
C11	0.342	0.0462	0.834	0.708	97 392	27 100
C12	0.363	0.0490	0.884	0.729	118 342	33 571
C13	0.400	0.0485	0.650	0.675	35 503	14 626
C14	0.406	0.0466	0.867	0.712	104 266	30 918
C15	0.428	0.0492	0.830	0.732	92 352	28 348
C15_norad	0.428	0.0492	0.830	0.732	79 399	25 270

Magneticum subgrid physics does reproduce realistic haloes,[1] thus one can assume that its concentration parameter is realistic and of general applicability for purposes of calibration on observational studies.

Table 1 gives an overview of the cosmological simulations used in this work. They have already been presented in Singh et al. (2019, see table 1 in their paper) and labelled as C1–15 and has a different configuration of the cosmological parameters Ω_m, Ω_b, h, and σ_8. Additionally, we use two simulations with the same set-up as C1 and C15, labelled respectively as C1_norad and C15_norad, that have been run without radiative cooling and star formation. Each simulation covers a volume of 896 Mpc h^{-1}, has a DM particle mass m_{DM}=1.3·10^{10}Msun/h, a gas particle mass m_{gas}=2.6·10^{9}Msun/h and a softening ε=10kpc/h.

For each simulation, we study the haloes at a timeslice with redshifts $z = 0.00,\ 0.14,\ 0.29,\ 0.47,\ 0.67$, and $z = 0.90$. In the following sections, we repeat the same analyses for overdensities Δ_{vir}, Δ_{200c}, Δ_{500c}, Δ_{2500c}, Δ_{200m} performing a corresponding mass cut (respectively on $M = M_{vir}, M_{200c}, M_{500c}, M_{2500c}, M_{200m}$) that ensures that all haloes have at least 10^4 particles. This cut is different for each of our simulations. This is opposed to what was used in Singh et al. (2019), where they choose a fixed mass cut for all C1–C15 simulations. The mass range of these haloes is between 10^{14} and 4×10^{15} $M_\odot$, which fits the typical range of GC weak-lensing masses (see e.g. Applegate et al. 2014).

[1]In particular, Magneticum simulations match observations of angular momentum for different morphologies (Teklu et al. 2015; Teklu, Remus & Dolag 2016); the mass–size relation (Remus & Dolag 2016; Remus et al. 2017; van de Sande et al. 2019); the dark matter fraction (see fig. 3 in Remus et al. 2017); the baryon conversion efficiency (see fig. 10 in Steinborn et al. 2015); kinematical observations of early-type galaxies (Schulze et al. 2018); the inner slope of the total matter density profile (see fig. 7 in Bellstedt et al. 2018), the ellipticity and velocity over velocity dispersion ratio (van de Sande et al. 2019); and reproduce the high concentration of high luminosity gap of fossil objects (Ragagnin et al. 2019).

In this work, we fit the NFW profile (see equation 1) over the *total matter component* (i.e. dark matter and baryons) as opposed to previous works (see Ragagnin et al. 2019), where the NFW profile fit was performed over the dark matter component only. We fit the density profile over 20 logarithmic bins, starting from $r = 100$ kpc (similar to the cut applied in observational studies as Dietrich et al. 2019). All fits with a $\chi^2 > 10^3$ have been excluded from our analyses (which accounts for a few hundred haloes per snapshot) as they correspond to heavily perturbed objects. Although works on simulations typically present quantities in comoving units of h, unless differently specified, all masses and distances presented in this manuscript are in physical units.

3 HALO CONCENTRATIONS

In Appendix A, we study the effect of baryons on Mc planes and show how an incorrect treatment of baryons can lead to underestimation of the concentration up to 20 per cent and how the interplay between dark matter and baryons put the dynamical state of hydrodynamic simulations in a much more complex picture than the one of DMO simulations.

This motivates us to study halo masses and concentrations on hydrodynamic simulations, and in particular we focus on their dependence on cosmological parameters. We perform a fit of the concentration as a function of mass and redshift for each simulation at each overdensity of Magneticum simulations. The functional form of the concentration is chosen as a power law on mass and scale factor as done in the observational studies (see e.g. Merten et al. 2015) as

$$\ln c_\Delta(M_\Delta) = \ln A + B \ln\left(\frac{M_\Delta}{M_p}\right) + C \ln\left(\frac{a}{a_p}\right) + \sigma. \quad (5)$$

Here, A and B are fit parameters, σ is the logarithmic scatter, and a_p and M_p are median of mass and scale factor, respectively, and are used as pivot values.

We maximized the following likelihood $\hat{\mathcal{L}}$[2] with a uniform prior for all fit parameters:

$$\ln \hat{\mathcal{L}} = -\frac{1}{2}\left(\ln(2\pi\sigma^2) + \left(\frac{\ln c_\Delta\,(M_\Delta, A, B, C) - \ln c_\Delta}{\sigma}\right)^2\right). \quad (6)$$

Fig. 1 shows the Mc planes for $\Delta_{\rm vir}$ (computed following equation 2) for all 15 simulations, together with the concentration from the redshift–mass–concentration (aMc relation) colour coded by $\log_{10}\chi^2$. Haloes with high χ^2 tend to have lower concentration which qualitatively agrees with other theoretical studies that show how perturbed objects have lower concentrations (see e.g. Balmès et al. 2014; Ludlow et al. 2014; Klypin et al. 2016). For this reason, in an Mc plane, it is not advisable to weight halo concentrations with $1/\chi^2$, as this would bias the relation towards higher concentrations. Although the concentration is believed to decrease with increasing halo mass, extreme cosmologies such as C1 and C2 (with $\Omega_{\rm m} < 0.2$) have an overall positive dependence between the mass and concentration. On the other hand, the logarithmic mean slope is low (between -0.03 and 0.08) and its influence in the Mc plane is not dominant in our mass regime of interest.

3.1 Comparison with other studies

We then compare Magneticum simulation concentrations of haloes with the concentration predicted by the Cosmic Emulator (Bhattacharya et al. 2013; Heitmann et al. 2016). The Cosmic Emulator is a tool to predict the Mc planes for a given wCDM. We were able to compare only C7, C8, and C9 cosmologies because the other Magneticum simulations had cosmological parameters that were out of the range of the Cosmic Emulator. Note that while the Cosmic Emulator dependence on $\Omega_{\rm b}$ is encoded in the power spectrum normalization, our Mc relation dependence on $\Omega_{\rm b}$ takes into account all physical processes of baryon physics, including star formation and feedback.

The ratio of median concentration $c_{\rm vir}$ parameters of haloes obtained with our Mc fit and the concentration provided by the Cosmic Emulator is $\approx$1.2. We notice how the Cosmic Emulator concentrations (retrieved by DMO runs) are systematically higher than Magneticum simulations in this mass regime (by a factor of $\approx$ 10–20 per cent), in agreement with our comparison in Ragagnin et al. (2019). The scatter is constant over mass, redshift, and cosmology, to nearly $\sigma \approx 0.38$, in agreement with the value of $\approx$1/3 presented in the wCDM DMO model of Kwan et al. (2013).

Fig. 2 shows the Mc plane for the full-physics simulations C1–15 against other DMO simulations and observations. We compare our mass-concentration planes with results from Omega500 simulations (Shirasaki et al. 2018); CLASH concentrations from Merten et al. (2015), numerical predictions from MUSIC of CLASH (Meneghetti et al. 2014), where a number of simulated haloes have been chosen to make mock CLASH observations. To highlight the high scatter in the mass-concentration relation, we show high concentration groups from Pratt et al. (2016) and an under-luminous and low-concentration halo presented in Andreon et al. (2019). When analysing this data, one must be aware of their selection effects: CLASH data set underwent some filtering difficult to model, while fossil objects presented in Pratt et al. (2016) by construction lay in the upper part of the Mc plane. There is a general agreement between concentration of Magneticum simulations and these observations.

[2]We used the PYTHON package EMCEE (Foreman-Mackey et al. 2013).

4 COSMOLOGY DEPENDENCE OF CONCENTRATION PARAMETER

The 15 cosmologies we use in this work have different Mc normalization values and log-slope (see Fig. 1). We perform a fit of the concentration as a function of mass, scale factor, and cosmological parameters in order to interpolate an Mc plane at a given, arbitrary, cosmology, i.e. a concentration $c_\Delta\,(M_\Delta, 1/(1+z), \Omega_{\rm m}, \Omega_{\rm b}, \sigma_8, h_0)$. As the intrinsic scatter is constant (within few per cents), we did not further parametrize it and assumed it to be independent of mass, redshift, and cosmology. The functional form of the fit parameters in equation (5), with a dependence on cosmology is as follows:

$$\begin{aligned}
A &= A_0 + \alpha_{\rm m}\ln\left(\frac{\Omega_{\rm m}}{\Omega_{\rm m,p}}\right) + \alpha_{\rm b}\ln\left(\frac{\Omega_{\rm b}}{\Omega_{\rm b,p}}\right) + \\
&\quad + \alpha_\sigma \ln\left(\frac{\sigma_8}{\sigma_{8,\rm p}}\right) + \alpha_{\rm h}\ln\left(\frac{h_0}{h_{0,\rm p}}\right) \\
B &= B_0 + \beta_{\rm m}\ln\left(\frac{\Omega_{\rm m}}{\Omega_{\rm m,p}}\right) + \beta_{\rm b}\ln\left(\frac{\Omega_{\rm b}}{\Omega_{\rm b,p}}\right) + \\
&\quad + \beta_\sigma \ln\left(\frac{\sigma_8}{\sigma_{8,\rm p}}\right) + \beta_{\rm h}\ln\left(\frac{h_0}{h_{0,\rm p}}\right) \\
C &= C_0 + \gamma_{\rm m}\ln\left(\frac{\Omega_{\rm m}}{\Omega_{\rm m,p}}\right) + \gamma_{\rm b}\ln\left(\frac{\Omega_{\rm b}}{\Omega_{\rm b,p}}\right) + \\
&\quad + \gamma_\sigma \ln\left(\frac{\sigma_8}{\sigma_{8,\rm p}}\right) + \gamma_{\rm h}\ln\left(\frac{h_0}{h_{0,\rm p}}\right).
\end{aligned} \quad (7)$$

The fit has been performed for $\Delta = \Delta_{\rm vir}$, Δ_{200c}, Δ_{500c}, Δ_{2500c}, and Δ_{200m} by maximizing the Likelihood as in equation (6). Table 2 shows the results with cosmological parameter pivots at the reference cosmology C8.

Given the high number of free parameters, in order to not underestimate possible sources of errors in the fit, we decided to evaluated uncertainties as follows in Singh et al. (2019): (1) we first reperformed the fit for each simulation by setting its own cosmological parameter as pivot values; (2) then for each parameter except A_0, B_0, C_0, we considered the standard deviation of the parameter values in the previous fits and set it as uncertainty in Table 2; (3) parameters A_0, B_0, C_0 are presented without uncertainty because the error obtained from the Hessian matrix is negligible compared to the scatter parameter σ. Being this work first necessary step towards a cosmology-dependent Mc relation, these parameters may be constrained with more precision in future simulation campaigns.

From the above fit, we find that the normalization (α parameters) is mainly affected by $\Omega_{\rm m}$ and σ_8. The slope of the Mc plane (β parameters) has a weak dependence on cosmology. However, the logarithmic mass slope is pushed towards negative values by an increase in $\Omega_{\rm m}$ and h_0 (i.e. $\beta_{\rm m}$ and $\beta_{\rm h} < 0$), while it is pushed towards positive values by an increase in $\Omega_{\rm b}$ and σ_8 (since $\beta_{\rm b}$ and $\beta_\sigma > 0$). This behaviour is also shown in Fig. 2. Note that, C1 and C2 have opposite mass dependence with respect to the other runs. Although the trend can be positive for some cosmologies (see Table 2 and Fig. 1), the slope is always close to zero. The redshift dependence (γ parameters) is driven by both σ_8 and $\Omega_{\rm m}$, while a high baryon fraction can lower the dependence (see parameter $\gamma_{\rm h}$). The scatter is nearly constant for all the overdensities with a value close to 0.38 and even if it is of the same order of the difference between Mc relations of different cosmologies (see shaded area in Fig. 2), in the next subsection we will show that statistical studies on large

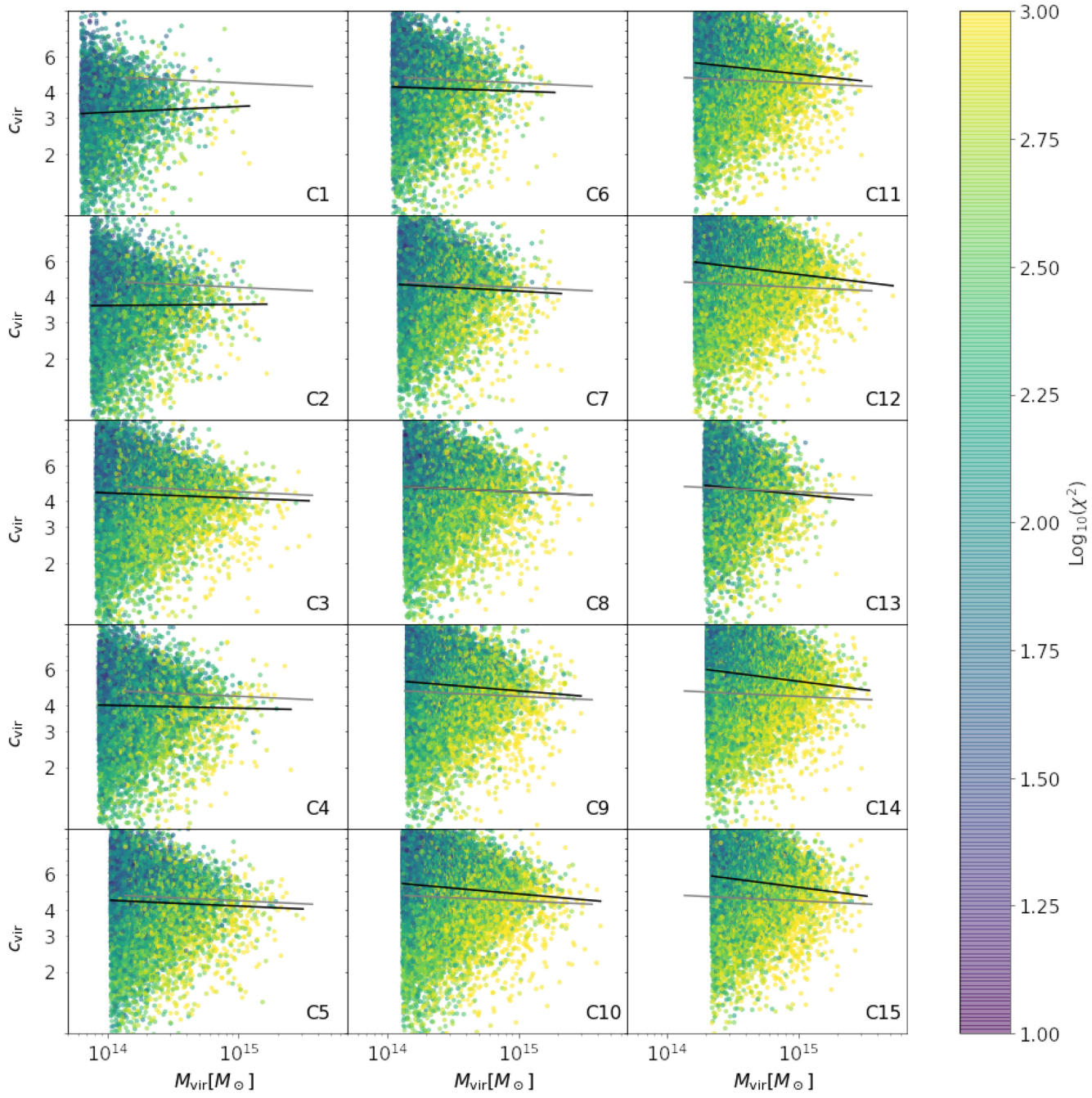

Figure 1. Each panel shows the Mc plane one full physics Magneticum simulation presented in Table 1. Concentrations are computed at overdensity Δ_{vir}. Data points represent all selected haloes at redshift $z = 0$, colour coded by their $\log_{10}\chi^2$. Concentration values are plotted only in the range $c_{vir} = 1 - 10$, because this range contains vast majority of haloes. Black line corresponds to the Mc relation obtained by the fit in equation (5). Grey lines correspond to the Mc relation obtained for the simulation C8 (which uses the reference cosmology; Komatsu et al. 2009). The different mass cut on each panel is due to our choice of selecting the smallest mass cut where all haloes have at least 10^4 particles. As a consequence, our mass cuts depend on cosmological parameters.

samples of GCs are still affected by the cosmological dependence of Mc relations.

Since the logarithmic slope of the mass has a weak dependence on cosmology, we provide a similar fit as the one in this section without B having any cosmological dependences i.e. $B = B_0$ in Appendix B (see Table B1). In Appendix B (see Table B2), we also provide the same reduced fit parameters with the scale radius computed on the dark matter density profile.

4.1 Impact on inferred weak-lensing masses

There are differences between the Mc relation extracted from our simulations at different cosmologies and the ones from DMO simulations. When Mc relations are used to provide priors and interpret the weak-lensing signal of non-ideal NFW cluster samples, the different Mc relations will ultimately lead to different inferred masses and therefore different cosmological constraints from cluster number count experiments. In fact, works such as Henson et al.

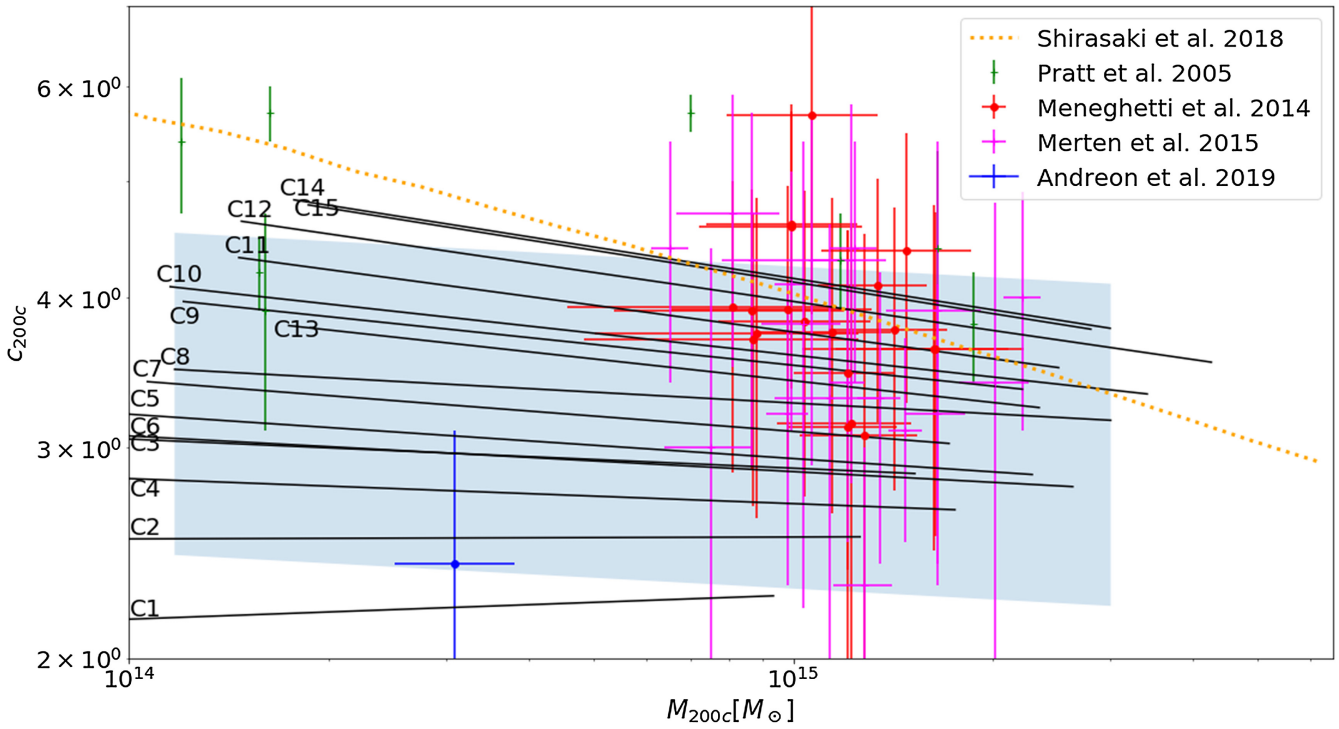

Figure 2. Mc plane of our simulations C1–C15 (black solid lines), haloes from the hydrodynamic cosmological simulation Omega500 (Shirasaki et al. 2018; dashed orange line), observations of fossil groups from Pratt et al. (2016; orange data points), mock observations from Meneghetti et al. (2014; red data points), data from CLASH (Meneghetti et al. 2014; magenta data points) and a low-concentration halo from Andreon et al. (2019; blue data point). Shaded area is the scatter around the C8 relation.

Table 2. Pivots and best-fitting parameters for the cosmology–redshift–mass–concentration plane and its dependence on cosmology as in equations (5) and (7) for concentration overdensities of $\Delta = \Delta_{\rm vir}$, Δ_{200c}, Δ_{500c}, Δ_{2500c}, and Δ_{200m}. The pivots $\Omega_{\rm m,p}$, $\Omega_{\rm b,p}$, σ_8, and h_0 in equation (7) are the cosmological parameters of C8 as in Table 1 ($\Omega_{\rm m} = 0.272$, $\Omega_{\rm b} = 0.0456$, $\sigma_8 = 0.809$, $h_0 = 0.704$). Pivots $a_{\rm p}$ and $M_{\rm p}$ are, respectively, median of scale factor and mass of all haloes. Errors on A_0, B_0, C_0, and σ are omitted as they are all < 0.001 per cent. The package HYDRO_MC contains a script that utilizes this relation (#1).

Param.	Overdensity				
	vir	200c	500c	2500c	200m
$M_{\rm p}$ ($M_\odot$)	19.9×10^{13}	17.4×10^{13}	13.7×10^{13}	6.9×10^{13}	22.4×10^{13}
$a_{\rm p}$	0.877	0.877	0.877	0.877	0.877
A_0	1.50	1.24	0.86	0.13	1.69
B_0	−0.04	−0.05	−0.05	−0.03	−0.04
C_0	0.52	0.20	0.19	0.11	0.91
$\alpha_{\rm m}$	0.454 ± 0.041	0.632 ± 0.042	0.662 ± 0.042	0.759 ± 0.055	0.227 ± 0.037
$\alpha_{\rm b}$	-0.249 ± 0.040	-0.246 ± 0.038	-0.235 ± 0.049	-0.272 ± 0.134	-0.266 ± 0.035
α_σ	0.554 ± 0.030	0.561 ± 0.034	0.519 ± 0.047	0.422 ± 0.050	0.528 ± 0.022
$\alpha_{\rm h}$	-0.005 ± 0.030	-0.026 ± 0.016	-0.031 ± 0.065	-0.021 ± 0.167	0.016 ± 0.028
$\beta_{\rm m}$	-0.122 ± 0.001	-0.118 ± 0.001	-0.112 ± 0.001	-0.116 ± 0.001	-0.116 ± 0.001
$\beta_{\rm b}$	0.117 ± 0.005	0.112 ± 0.004	0.126 ± 0.005	0.289 ± 0.007	0.115 ± 0.008
β_σ	0.051 ± 0.003	0.056 ± 0.002	0.088 ± 0.004	0.103 ± 0.005	0.050 ± 0.006
$\beta_{\rm h}$	-0.079 ± 0.013	-0.044 ± 0.009	-0.156 ± 0.014	-0.342 ± 0.017	-0.094 ± 0.027
$\gamma_{\rm m}$	0.240 ± 0.006	0.352 ± 0.007	0.346 ± 0.009	0.384 ± 0.011	-0.043 ± 0.009
$\gamma_{\rm b}$	-0.126 ± 0.034	-0.039 ± 0.040	-0.045 ± 0.051	-0.133 ± 0.062	-0.063 ± 0.053
γ_σ	0.664 ± 0.027	0.767 ± 0.026	0.856 ± 0.032	0.846 ± 0.046	0.635 ± 0.039
$\gamma_{\rm h}$	-0.030 ± 0.109	-0.276 ± 0.112	-0.347 ± 0.136	0.003 ± 0.171	-0.405 ± 0.135
σ	0.388 ± 0.001	0.384 ± 0.001	0.377 ± 0.001	0.383 ± 0.001	0.388 ± 0.001

(2017) show that it is possible to correctly recover halo masses from mock observations of both DMO and hydrosimulations by using their respective Mc relations. On the other hand, in low signal-to-noise conditions, weak-lensing mass calibration typically constrains the total observed mass using Mc relations derived from DMO simulations (see e.g. Melchior et al. 2017). In the following, we quantify and discuss this effect on a simplified example.

To this end, we create a simulated projected surface density profile of an NFW model of the RXC J2248.7−4431 cluster (Gruen et al. 2013), at $z = 0.436$ with mass $M_{200c} = 1.75 \cdot 10^{15}\,\mathrm{M}_\odot$ (Melchior et al. 2015). The simulated profile is generated using equation (41) in Łokas & Mamon (2001) with a concentration c_{200c} from our Mc relation (see Table 2) and with cosmological parameters $\Omega_\mathrm{m} = 0.27$, $\Omega_\mathrm{b} = 0.05$, $\sigma_8 = 0.8$, $h_0 = 0.67$. We mimic a simplified observed radial profile sampled with 20 logarithmic equally spaced radial bins from 3 to 30 arcmin. To each data point, we assigned an associated error in order to simulate typical weak-lensing observational conditions (S/N = 5) of a massive clusters in a photometric survey like the Dark Energy Survey (DES; Melchior et al. 2015). We test a simplified mass calibration process by fitting the above described density profile with a Gaussian likelihood for each simulated projected density radial bin Σ_i:

$$\mathcal{L} = \prod_i P(\Sigma_i | M_{200c}, c_{200c}, \Delta_{\Sigma,i}). \tag{8}$$

We adopt a flat prior on $\log M_{200c}$ and test the impact of adopting the following different priors for the concentration:

(i) Ragagnin20: The Mc relation with a lognormal scatter $\sigma_{\ln c|M} = 0.38$ as presented in this work.
(ii) Diemer19: The DMO Mc relation proposed in Diemer & Joyce (2019)[3] with a lognormal scatter $\sigma_{\ln c|M} = 0.39$.

To show the impact on mass calibration of Ragagnin20 and the dependence on cosmological parameters, we perform the calibration both at the correct input cosmology (from here on Cosmo A) and with cosmological parameters randomly extracted from the posterior distribution of the cosmological parameters derived by SPT cluster number counts (Bocquet et al. 2019; $\Omega_\mathrm{m} = 0.26$, $\Omega_\mathrm{b} = 0.04$, $\sigma_8 = 0.6$, $h_0 = 0.66$ from here on Cosmo B).

Fig. 3 (top panel) shows the ideal unperturbed mock profile and best-fitting realizations of NFW profiles produced using Ragagnin20 (red line) and Diemer19 (blue line). The Mc relation presented in this work has a lower concentration normalization than Diemer19 (Appendix A), and thus Ragagnin20 produces lower values of surface densities near the centre and higher values on the outskirts with respect to DMO Mc relations. Different prior assumptions on the Mc relation affect the inferred mass, as we see in Fig. 3 (middle panel).[4] While the posterior derived assuming the Mc relations of Ragagnin20 and of Diemer19 are in good agreement, the best-fitting mass recovered with Diemer19 is ≈ 10 per cent higher compared to the one derived with Ragagnin20. This can be better appreciated in the bottom panel of Fig. 3, where we instead simulate the mass calibration of a stack of 100 clusters (Melchior et al. 2017). We therefore mimic an S/N = 50 stacked average profile and decrease by a factor of $\sqrt{100}$ the intrinsic scatter around the Mc relation in the prior. Assuming the wrong Cosmo B cosmology, we would recover biased results using both the Ragagnin20 and the Diemer19 Mc relation, even if the marginalized posterior on the mass would be almost unbiased for the Ragagnin20 analysis. Furthermore we note that fixing Cosmo B cosmolgy instead of the correct input Cosmo A cosmolgy would result in a slightly smaller mass for Ragagnin20 and in a slightly larger mass for Diemer19. While a more sophisticated analysis including a treatment of systematic uncertainties and a self-consistent exploration of the cosmological parameters is beyond the purpose of this work, this simple exercise highlights the importance

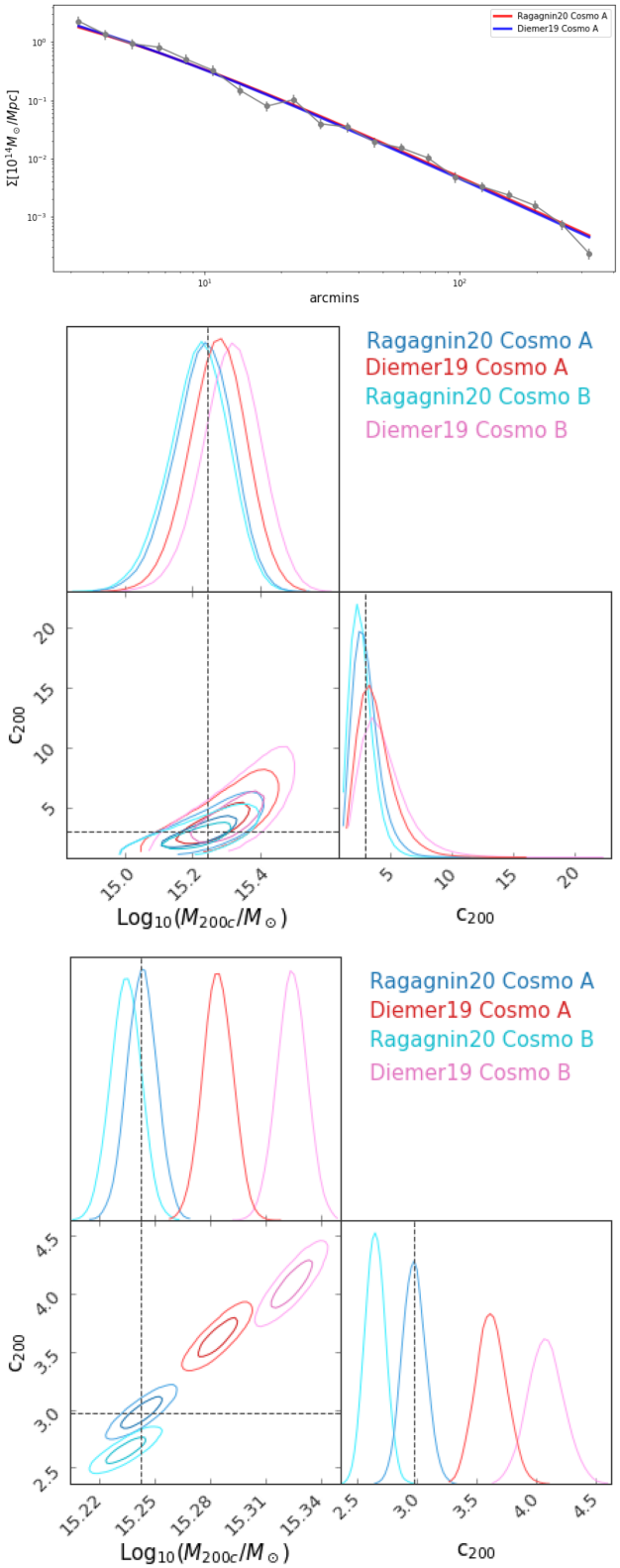

Figure 3. Top panel: Surface density of mock data points (grey line), and best-fitting realizations with DMO Mc relation priors (red line) and this work (blue line). Middle and bottom panel: Marginalized posterior parameter distributions of $\log_{10} M_{200c}$ and c_{200}, with DMO Mc relation (red and pink lines) and this work's Mc relation (blue and cyan lines) for a simulated analysis of a single observation (middle panel) and of a stack of 100 GCs (bottom panel).

[3]We used the PYTHON package #1 (see Diemer 2018).
[4]Parameter space is sampled with EMCEE.

of a correct modelization of the cosmological dependence of the Mc relation in the the weak-lensing analysis of cluster samples for cosmological purposes.

We stress that in this experiment, we wanted to mimic the procedure of most observational works, thus we did not model baryon component of DMO simulations.

5 HALO MASSES CONVERSION

In the following subsections, we present and compare different methods of converting masses between overdensities. We also provide a direct fit for converting masses (i.e. SUBFIND masses) from $\Delta 1$ to $\Delta 2$ (thus without using the Mc relation), in order to study the origin of the scatter coming from the conversions. This kind of conversions is used in computing the sparsity of haloes (i.e. ratio of masses in two overdensities), which itself can probe cosmological parameters (Corasaniti et al. 2018; Corasaniti & Rasera 2019) and dark energy models (Balmès et al. 2014).

5.1 Mass–mass conversion using Mc relation

In this section, we tackle the problem of converting masses via an Mc relation. By combining the definition of mass M_Δ (see equation 4) and the fact that the matter profile only depends on a proportional parameter ρ_0 and a scale radius r_s, we get

$$M_\Delta = 4\pi\rho_0 r_s^3 f(c_\Delta) = \Delta\frac{4}{3}\pi R_\Delta^3\rho_c. \tag{9}$$

For an NFW profile as in equation (1),

$$f(c_\Delta) = \ln(1+c_\Delta) - \frac{c_\Delta}{1+c_\Delta}. \tag{10}$$

Combining equations (9) and (10) gives the following mass conversion formula:

$$\begin{cases} M_{\Delta 2} = M_{\Delta 1}\left(\frac{c_{\Delta 2}}{c_{\Delta 1}}\right)^3\frac{\Delta_2}{\Delta_1} \\ c_{\Delta,2} = c_{\Delta,1}\cdot\left(\frac{\Delta_1}{\Delta_2}\frac{f(c_{\Delta,2})}{f(c_{\Delta,1})}\right)^{\frac{1}{3}}. \end{cases} \tag{11}$$

From the second part of equation (11), it is possible to evaluate the concentration $c_{\Delta 2}$ as a function of only $c_{\Delta 1}$ (as in appendix C of Hu & Kravtsov 2003).

Equation (11) can be used to estimate the theoretical scatter $\sigma_{\rm theo}$ obtained in the mass conversion by analytically propagating the uncertainties of the Mc relation, namely:

$$\sigma_{\rm theo} = \frac{1}{M_{\Delta 2}}\frac{{\rm d}M_{\Delta 2}}{{\rm d}c_{\Delta 1}}\sigma_{c,\Delta 1}, \tag{12}$$

where $M_{\Delta 2}$ is the converted mass, $c_{\Delta 1}$ the concentration in the original overdensity Δ_1, and $\sigma_{c,\Delta 1}$ is the uncertainty in the concentration (in our case it is the scatter in the Mc relation). Appendix C describes how to obtain the theoretical scatter one would expect given a perfectly NFW profile.

There are several sources of error in the mass–mass conversion derived by an Mc relation: (i) the intrinsic scatter of the Mc relation, (ii) the fact that profiles are not perfectly NFW and thus equation (10) is not the best choice for this conversion; and (iii) the cosmology–redshift–mass–concentration fit (as in Table 2) may not be optimal.

To further study the sources of uncertainties in this conversion, we fit SUBFIND halo masses between two overdensities,[5] and compare the two conversion methods.

5.2 $M_{\Delta 1}$–$M_{\Delta 2}$ (M–M) plane

In this subsection, we perform a direct fit between halo masses (i.e. SUBFIND masses), as a function of redshift and cosmological parameter. The reason of this fit is twofold: (1) we want to study the uncertainty introduced in the conversion of the previous subsection and (2) we want to provide a way of converting masses without any assumption on their concentration and NFW density profile.

For each pair of overdensities, we performed a fit of the mass $M_{\Delta 2}(M_{\Delta 1}, 1/(1+z), \Omega_{\rm m}, \Omega_{\rm b}, \sigma_8, h_0)$ with the following functional form:

$$\ln M_{\Delta 2}(M_{\Delta 1}, a) = \ln A + B\ln\left(\frac{M_{\Delta 1}}{M_{\rm p}}\right) + C\ln\left(\frac{a}{a_{\rm p}}\right), \tag{13}$$

where A, B, C parameters are parametrized with cosmology as in equation (7).

Table 3 shows the results of the mass–mass conversion fit between critical overdensities, while Table 4 shows the conversion fit parameters between Δ_{200c} and Δ_{200m}. The conversion relation has a strong dependence on σ_8 and a weak dependence on h_0 (see $\alpha_{\rm m}$, $\beta_{\rm m}$, $\gamma_{\rm m}$ parameters).

5.3 Uncertainties in mass conversions

When converting between masses at different overdensities, we are interested in the following sources of uncertainty:

(i) $\sigma_{\rm M–M(Mc)}$: the scatter from the mass–mass conversion obtained with the aid of our Mc relation found in Section 5.1.

(ii) $\sigma_{\rm M–M(}_{c}{\rm)}$: the scatter obtained from a conversion between the true values of $M_{\Delta 1}$ and $c_{\Delta 1}$ of a given halo to $M_{\Delta 2}$ (i.e. using only equation 11). We use this scatter in order to estimate the error coming from non-NFWness (i.e. deviation from perfect NFW density profile).

(iii) $\sigma_{\rm theo}$: the scatter obtained by analytically propagating the Mc log-scatter ($\approx$0.38 as in Table 2) with equation (12). This value estimates the uncertainty coming from the intrinsic scatter of the Mc relation alone.

(iv) $\tilde{\sigma}_{\rm Mc}$: the scatter that is supposed to be introduced by a non-ideal cosmology–redshift–mass–concentration fitting formula.

(v) $\sigma_{\rm M–M}$: the intrinsic scatter of M–M conversion using Table 3 presented in Section 5.2.

In a simplistic approach, the quadrature sum of the scatter coming from non-NFWness ($\sigma_{\rm M–M(}_{c}{\rm)}$), the theoretical scatter ($\sigma_{\rm theo}$) and the scatter due to a non-ideal Mc fit ($\tilde{\sigma}_{\rm Mc}$), should all add up to the scatter in the mass–mass conversion using an Mc relation:

$$\sigma^2_{\rm M–M(Mc)} = \sigma^2_{\rm M–M(}_{c}{\rm)} + \sigma^2_{\rm theo} + \tilde{\sigma}^2_{\rm Mc}. \tag{14}$$

5.4 Obtaining M_{200c} from M_{500c} or M_{2500c}

In this subsection, we test mass conversion to M_{200c} given M_{500c} or M_{500c}. We compare results obtained using the technique described in Section 5.1 against the mass–mass relation from equation (13).

[5]The package HYDRO_MC contains a sample script to convert masses between two overdensities by using the Mc relation presented in this paper (#1).

Table 3. Fit parameters for equations (13) and (7) for overdensities $\Delta_{\rm vir}$, Δ_{200c}, Δ_{500c}, Δ_{2500c}, and Δ_{200m}. Pivots are as in Table 2. Errors on A_0, B_0, C_0, and σ are omitted as they are all < 0.001 per cent. The package HYDRO_MC contains a script that utilizes this relation (#1).

Param.	From overdensity → to overdensity					
	vir → 200c	vir → 500c	vir → 2500c	200c → vir	200c → 500c	200c → 2500c
$M_{\rm p}$ ($\rm M_\odot$)	19.9×10^{13}	19.9×10^{13}	19.9×10^{13}	17.4×10^{13}	17.4×10^{13}	17.4×10^{13}
$a_{\rm p}$	0.877	0.877	0.877	0.877	0.877	0.877
A_0	32.72	32.31	31.34	32.99	32.39	31.41
B_0	1.00	1.00	0.93	0.99	0.99	0.92
C_0	−0.24	−0.24	−0.01	0.23	0.00	0.22
$\alpha_{\rm m}$	0.165 ± 0.007	0.295 ± 0.015	0.619 ± 0.026	-0.156 ± 0.006	0.125 ± 0.009	0.461 ± 0.021
$\alpha_{\rm b}$	0.003 ± 0.011	-0.020 ± 0.033	-0.162 ± 0.069	-0.003 ± 0.009	-0.020 ± 0.023	-0.150 ± 0.062
α_σ	0.048 ± 0.008	0.177 ± 0.016	0.574 ± 0.016	-0.035 ± 0.006	0.120 ± 0.009	0.539 ± 0.016
$\alpha_{\rm h}$	-0.045 ± 0.004	-0.105 ± 0.013	-0.054 ± 0.068	0.037 ± 0.005	-0.060 ± 0.012	-0.042 ± 0.065
$\beta_{\rm m}$	-0.016 ± 0.001	-0.043 ± 0.001	-0.076 ± 0.001	0.015 ± 0.001	-0.025 ± 0.001	-0.058 ± 0.001
$\beta_{\rm b}$	0.030 ± 0.001	0.096 ± 0.003	0.203 ± 0.004	-0.026 ± 0.001	0.062 ± 0.003	0.171 ± 0.003
β_σ	-0.024 ± 0.001	-0.043 ± 0.002	-0.010 ± 0.003	0.017 ± 0.001	-0.020 ± 0.002	0.006 ± 0.002
$\beta_{\rm h}$	-0.007 ± 0.003	-0.038 ± 0.008	-0.203 ± 0.009	0.015 ± 0.003	-0.025 ± 0.009	-0.180 ± 0.009
$\gamma_{\rm m}$	0.159 ± 0.001	0.213 ± 0.002	0.379 ± 0.001	-0.153 ± 0.002	0.052 ± 0.003	0.211 ± 0.002
$\gamma_{\rm b}$	-0.050 ± 0.005	-0.115 ± 0.010	-0.232 ± 0.006	0.057 ± 0.009	-0.052 ± 0.016	-0.080 ± 0.013
γ_σ	0.123 ± 0.003	0.354 ± 0.009	0.555 ± 0.009	-0.107 ± 0.005	0.244 ± 0.007	0.486 ± 0.005
$\gamma_{\rm h}$	0.036 ± 0.011	0.026 ± 0.034	0.039 ± 0.035	-0.035 ± 0.019	-0.038 ± 0.029	-0.175 ± 0.031
σ	0.065 ± 0.001	0.158 ± 0.001	-0.312 ± 0.001	0.056 ± 0.001	0.113 ± 0.001	-0.296 ± 0.001
Param.	From overdensity → to overdensity					
	500c → vir	500c → 200c	500c → 2500c	2500c → vir	2500c → 200c	200c → 500c
	500c − vir	500c − 200c	500c − 2500c	2500c − vir	2500c − 200c	2500c − 500c
$M_{\rm p}$ ($M_\odot$)	13.7×10^{13}	13.7×10^{13}	13.7×10^{13}	6.9×10^{13}	6.9×10^{13}	6.9×10^{13}
$a_{\rm p}$	0.877	0.877	0.877	0.877	0.877	0.877
A_0	33.12	32.93	31.58	33.33	33.14	32.77
B_0	0.99	1.00	0.93	1.02	1.03	1.03
C_0	0.25	0.02	0.22	0.16	−0.08	−0.10
$\alpha_{\rm m}$	-0.264 ± 0.013	-0.114 ± 0.007	0.335 ± 0.012	-0.563 ± 0.030	-0.414 ± 0.023	-0.307 ± 0.014
$\alpha_{\rm b}$	0.003 ± 0.031	0.006 ± 0.021	-0.125 ± 0.045	0.093 ± 0.142	0.100 ± 0.126	0.090 ± 0.091
α_σ	-0.111 ± 0.015	-0.088 ± 0.009	0.409 ± 0.016	-0.342 ± 0.009	-0.316 ± 0.017	-0.255 ± 0.022
$\alpha_{\rm h}$	0.084 ± 0.025	0.058 ± 0.019	0.015 ± 0.080	0.103 ± 0.195	0.066 ± 0.184	0.019 ± 0.155
$\beta_{\rm m}$	0.034 ± 0.001	0.019 ± 0.001	-0.033 ± 0.001	0.063 ± 0.001	0.049 ± 0.001	0.029 ± 0.001
$\beta_{\rm b}$	-0.083 ± 0.005	-0.053 ± 0.002	0.115 ± 0.002	-0.300 ± 0.001	-0.264 ± 0.003	-0.189 ± 0.003
β_σ	0.033 ± 0.003	0.019 ± 0.001	0.031 ± 0.001	-0.019 ± 0.001	-0.035 ± 0.002	-0.045 ± 0.001
$\beta_{\rm h}$	0.064 ± 0.012	0.036 ± 0.005	-0.197 ± 0.005	0.412 ± 0.003	0.382 ± 0.007	0.320 ± 0.006
$\gamma_{\rm m}$	-0.190 ± 0.002	-0.033 ± 0.002	0.162 ± 0.001	-0.306 ± 0.001	-0.159 ± 0.001	-0.134 ± 0.003
$\gamma_{\rm b}$	0.101 ± 0.009	0.005 ± 0.012	-0.081 ± 0.005	0.152 ± 0.005	0.075 ± 0.010	0.047 ± 0.018
γ_σ	-0.373 ± 0.006	-0.281 ± 0.008	0.223 ± 0.003	-0.638 ± 0.008	-0.532 ± 0.014	-0.268 ± 0.010
$\gamma_{\rm h}$	-0.017 ± 0.023	0.130 ± 0.033	-0.083 ± 0.012	0.037 ± 0.024	0.147 ± 0.038	0.043 ± 0.042
σ	0.129 ± 0.001	0.096 ± 0.001	-0.235 ± 0.001	0.242 ± 0.001	0.228 ± 0.001	0.182 ± 0.001

We tested the conversion $M_{500c} \to M_{200c}$ in the mass regime of $M_{200c} \approx 10^{14} - 10^{15}\,\rm M_\odot$ and found the following scatter values: $\sigma_{\rm M\text{–}M(Mc)} = 0.09$,$\sigma_{\rm M\text{–}M(c)} = 0.04$, and $\sigma_{\rm theo} = 0.07$ by converting masses using Section 5.1 and $\sigma_{\rm M\text{–}M} = 0.07$ by using conversion table in Section 5.2. We are confident to have all uncertainty sources under control because the quadrature sum of all scatters from conversion described in Section 5.2 (i.e. $\sqrt{\sigma^2_{\rm M\text{–}M(c)} + \sigma^2_{\rm theo}} = 0.09$) equals $\sigma_{\rm M\text{–}M(Mc)}$ from Section 5.1 as in equation (14).

We repeat the same conversion for $M_{2500c} \to M_{200c}$ and find the following scatter values: $\sigma_{\rm M\text{–}M(Mc)} = 0.29$, $\sigma_{\rm M\text{–}M(c)} = 0.07$, $\sigma_{\rm theo} = 0.24$ by converting masses using Section 5.1 and $\sigma_{\rm M\text{–}M} = 0.22$, by using conversion table in Section 5.2. In this conversion, the quadrature sum of the theoretical scatters in equation (14) holds only if we attribute an additional source of the uncertainty to a non-ideal M_{2500c}–c_{2500c} relation fit $\tilde{\sigma}_{\rm Mc} = 0.14$.

This means that a direct mass–mass fit is more precise than a conversion that passes through an Mc relation when converting $M_{2500c} \to M_{200c}$.

It is interesting to see that in both scenarios the conversion with the lowest scatter is the one performed with the exact knowledge of both mass and concentration (i.e. $\sigma_{\rm M\text{–}M(c)}$ is the lowest). On the other hand, in the scenario where one only knows the mass of a halo, then the conversion with the lowest uncertainty is the one that uses relation in Section 5.2 (i.e. with a scatter $\sigma_{\rm M\text{–}M}$).

6 DISCUSSION ON COSMOLOGY DEPENDENCE OF MASSES AND CONCENTRATIONS

The concentration of haloes at fixed mass is a non-trivial function of cosmological parameters. We summarize in Fig. 4 (upper panel), the variation of c_{500c} as a function of cosmological parameters for a halo of mass $M_\Delta = 10^{14}\,\rm M_\odot$ to provide a more intuitive representation. In general, concentration normalization decreases with baryon fraction $\Omega_{\rm b}$. While a small (≈ 2 per cent) decrease is expected also on DMO models as Diemer & Joyce (2019), our

Table 4. Fit parameters for equations (13) and (7) between overdensities of Δ_{200c} to Δ_{200m}. Errors on A_0, B_0, C_0, and σ are omitted as they are all < 0.001 per cent. Pivots are as in Table 2. The package HYDRO_MC contains a script that utilizes this relation (#1).

Param	From overdensity → to overdensity	
	$200c \rightarrow 200m$	$200m \rightarrow 200c$
M_p ($M_\odot$)	17.4×10^{13}	22.4×10^{13}
a_p	0.877	0.877
A_0	33.11	32.71
B_0	0.99	1.01
C_0	0.46	−0.49
α_m	-0.288 ± 0.013	0.318 ± 0.016
α_b	-0.017 ± 0.015	0.014 ± 0.019
α_σ	-0.053 ± 0.011	0.088 ± 0.019
α_h	0.078 ± 0.009	-0.103 ± 0.003
β_m	0.031 ± 0.001	-0.035 ± 0.001
β_b	-0.040 ± 0.003	0.063 ± 0.003
β_σ	0.029 ± 0.002	-0.050 ± 0.002
β_h	0.017 ± 0.006	-0.011 ± 0.007
γ_m	-0.313 ± 0.002	0.358 ± 0.002
γ_b	0.062 ± 0.008	-0.102 ± 0.010
γ_σ	-0.201 ± 0.007	0.246 ± 0.010
γ_h	0.026 ± 0.022	0.033 ± 0.036
σ	0.084 ± 0.001	-0.102 ± 0.001

change in this mass range is likely associated with feedback from AGNs, as an increase of gas fraction implies more energy released by feedback processes, which is known to lower concentration. The logarithmic mass slope of the Mc (see Table 2) increases with Ω_b, in agreement with SNe feedback being less relevant in massive haloes. For concentration at $\Delta = 2500c$, the situation is less clear. $\Delta = 2500c$ is closer to the centre of the halo and depends more strongly on physical processes which are not solely regulated by gravity. The qualitative behaviour is nevertheless consistent with $\Delta = 500c$, with the strongest (positive) cosmological dependence on σ_8 and Ω_m, a weak (negative) dependence on Ω_b, and a weaker one on h_0. It is not possible to infer the effect of Ω_b on the redshift log-slope as its value is mainly driven by σ_8.

C1 and C2 simulations show a positive correlation between mass and concentration. This is in agreement with Prada et al. (2012), where they found that haloes with low rms fluctuation amplitude σ have a concentration that increases with mass. In fact, C1 and C2 have extremely low values of σ_8 (i.e. $\sigma_8 < 0.7$) which leads to low rms fluctuation amplitudes.

When converting masses from higher overdensities to lower overdensities, the scatter increases as the difference between overdensities increases (see Table 3). Fig. 4 (lower panel) shows the variation of sparsity normalization as a function of cosmological parameters. The log-slope of the mass dependence (β parameters) has almost no dependence on cosmology. One exception is made by $s_{200c,\,2500c}$, where normalization does depend on Ω_b. Note that this relation does not assume any density profile, thus this dependence cannot be caused by a bad NFW fit. This effect is probably due to baryon feedback that at this scale is capable of influencing the total matter density profile.

The redshift dependence (γ parameters) is mostly influenced by Ω_m and σ_8, with a contribution that increases with separation between overdensities, which may indicate a different growth of the internal and external regions of the halo.

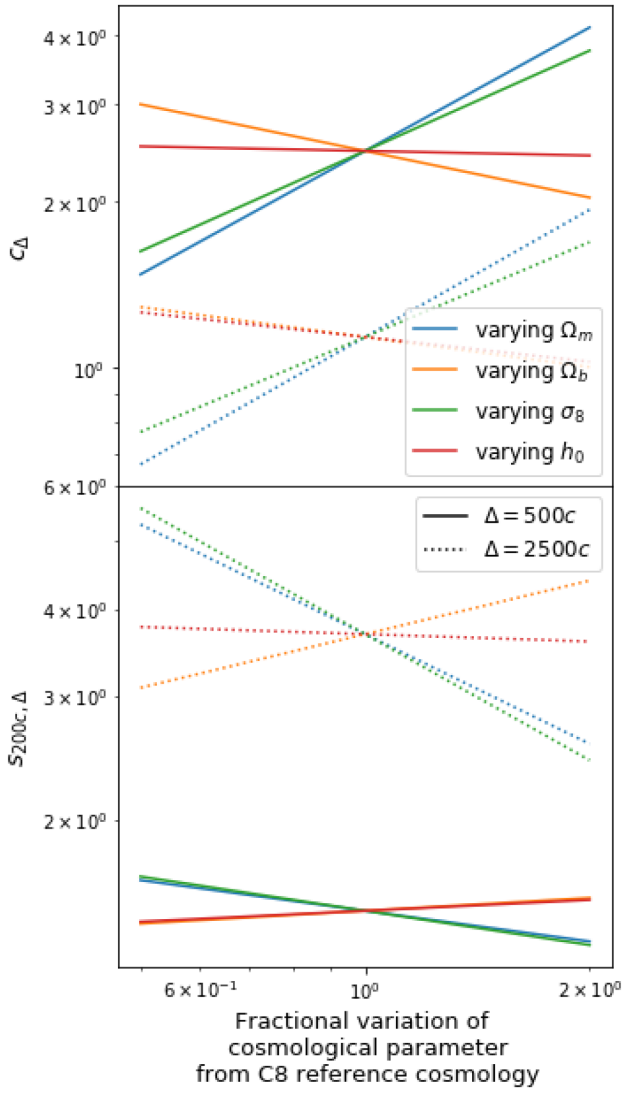

Figure 4. Change in concentration parameter (top panel) and sparsity (bottom panel) by fractional changes of cosmological parameters with respect to reference cosmology C8. Masses and sparsities are computing using our fit in Tables 2 and 3 for a halo of $M_\Delta = 10^{14}\,\mathrm{M}_\odot$.

7 CONCLUSIONS

We provided Mc relations and mass conversion relations between overdensities that include dependences on the cosmological parameters without modelling dynamical state of the simulated haloes. We showed that mass calibrated with DMO Mc relation can be ≈ 10 per cent higher compared with masses calibrated with our Mc relation. Additionally, cluster–cosmology oriented studies will benefit from this work since this relation averages over all different dynamical states and includes the average effect of baryon physics.

For these reasons, we performed the following studies:

(i) We provided the fitting functions for the cosmology–redshift–mass–concentration relation in the context of Magneticum hydrodynamic simulations for the critical overdensities Δ_vir, Δ_{200c}, Δ_{500c}, Δ_{2500c} and mean overdensity Δ_{200m} (see Section 4 and Table 2).

(ii) We explored the possibility of converting masses between overdensities with and without the aid of our Mc relation and, for

the latter, we studied the origin of its uncertainty as being caused by (i) non-NFWness of profiles and (ii) a non-ideal Mc fit. In particular, when converting masses via an Mc relation, non-NFWness of density profiles accounts for approx. 6 per cent of the scatter. Additionally the conversion between M_{2500} to M_{200} has an additional fractional scatter of $\approx$0.15 caused by the non-ideal Mc relation fit.

(iii) In Section 6, we discuss the dependence of halo masses and concentration as a function of cosmological parameters. Although concentration is mainly driven by $\Omega_{\rm m}$ and σ_8, we found that $\Omega_{\rm b}$ does decrease concentration and a higher h_0 lowers the concentration of the internal part of the halo, probably because of the related scale-dependent baryon feedback. We also found that the positive Mc trend in $C1$ and $C2$ is due to their low σ_8.

We released the PYTHON package HYDRO_MC (github.com/aragagnin/hydro_mc). This tool is able to perform all kinds of conversions presented in this paper and we provided a number of ready-to-use examples: Mc relation presented in Table 2 (#1), mass–mass conversion with fit parameters in Table 3 (#1), and mass–mass conversion through the Mc relation in Table 2 (#1).

ACKNOWLEDGEMENTS

The *Magneticum Pathfinder* simulations were partially performed at the Leibniz-Rechenzentrum with CPU time assigned to the Project 'pr86re'. AR received funding from the European Union's Horizon 2020 research and innovation programme EuroEXA under Grant Agreement no 754337. KD acknowledges support by DAAD contract number 57396842. AR acknowledges support by MIUR-DAAD contract number 34843 'The Universe in a Box'. AS and PS are supported by the ERC-StG 'ClustersXCosmo' grant agreement 716762. AS is supported by the FARE-MIUR grant 'ClustersXEuclid' R165SBKTMA and by INFN InDark grant. This work was supported by the Deutsche Forschungsgemeinschaft (DFG, German Research Foundation) under Germany's Excellence Strategy – EXC-2094-390783311. We are especially grateful for the support by M. Petkova through the Computational Center for Particle and Astrophysics (C^2PAP). Information on the *Magneticum Pathfinder* project is available at http://www.magneticum.org. We acknowledge the use of Bocquet & Carter (2016) PYTHON package to produce the MCMC plots. We thank the referee for the useful comments, which we believe significantly improved the clarity of the manuscript. We also thank Stefano Andreon for the useful feedback on this manuscript.

DATA AVAILABILITY

The data underlying this article will be shared on reasonable request to the corresponding author.

REFERENCES

Achitouv I., Baldi M., Puchwein E., Weller J., 2016, Phys. Rev. D, 93, 103522
Andreon S., Moretti A., Trinchieri G., Ishwara-Chand ra C. H., 2019, A&A, 630, A78
Applegate D. E. et al., 2014, MNRAS, 439, 48
Balmès I., Rasera Y., Corasaniti P. S., Alimi J. M., 2014, MNRAS, 437, 2328
Bartalucci I., Arnaud M., Pratt G. W., Démoclès J., Lovisari L., 2019, A&A, 628, A86
Baxter E. et al., 2016, MNRAS, 461, 4099
Beck A. M. et al., 2016, MNRAS, 455, 2110
Bellstedt S. et al., 2018, MNRAS, 476, 4543
Bhattacharya S., Habib S., Heitmann K., Vikhlinin A., 2013, ApJ, 766, 32
Biffi V., Dolag K., Böhringer H., 2013, MNRAS, 428, 1395
Biviano A. et al., 2017, A&A, 607, A81
Bocquet S., Carter F. W., 2016, J. Open Source Softw., 1
Bocquet S., Saro A., Dolag K., Mohr J. J., 2016, MNRAS, 456, 2361
Bocquet S. et al., 2019, ApJ, 878, 55
Boylan-Kolchin M., Springel V., White S. D. M., Jenkins A., Lemson G., 2009, MNRAS, 398, 1150
Brainerd T., 2019, American Astronomical Society Meeting Abstracts #233, p. 338.06
Bryan G. L., Norman M. L., 1998, ApJ, 495, 80
Bulbul E. et al., 2019, ApJ, 871, 50
Bullock J. S., Kolatt T. S., Sigad Y., Somerville R. S., Kravtsov A. V., Klypin A. A., Primack J. R., Dekel A., 2001, MNRAS, 321, 559
Buote D. A., Barth A. J., 2019, ApJ, 877, 91
Capasso R. et al., 2020, MNRAS, 494, 2736
Chandrasekhar S., 1961, Hydrodynamic and Hydromagnetic Stability. Clarendon Press, Oxford
Ciesielski K., 2007, Banach J. Math. Anal., 1, 1
Corasaniti P. S., Rasera Y., 2019, MNRAS, 487, 4382
Corasaniti P. S., Ettori S., Rasera Y., Sereno M., Amodeo S., Breton M. A., Ghirardini V., Eckert D., 2018, ApJ, 862, 40
Corsini E. M. et al., 2018, A&A, 618, A172
Costanzi M. et al., 2019, MNRAS, 488, 4779
Cui W., Power C., Borgani S., Knebe A., Lewis G. F., Murante G., Poole G. B., 2017, MNRAS, 464, 2502
De Boni C., 2013, PoS, Corfu2012, 059
De Boni C., Ettori S., Dolag K., Moscardini L., 2013, MNRAS, 428, 2921
Diemer B., 2018, ApJS, 239, 35
Diemer B., Joyce M., 2019, ApJ, 871, 168
Dietrich J. P. et al., 2014, MNRAS, 443, 1713
Dietrich J. P. et al., 2019, MNRAS, 483, 2871
Dodelson S., 2003, Modern Cosmology, Academic Press, Cambridge, Massachusetts
Dolag K., Bartelmann M., Perrotta F., Baccigalupi C., Moscardini L., Meneghetti M., Tormen G., 2004, A&A, 416, 853
Dolag K., Borgani S., Murante G., Springel V., 2009, MNRAS, 399, 497
Dolag K., Gaensler B. M., Beck A. M., Beck M. C., 2015, MNRAS, 451, 4277
Dolag K., Komatsu E., Sunyaev R., 2016, MNRAS, 463, 1797
Fabjan D., Borgani S., Tornatore L., Saro A., Murante G., Dolag K., 2010, MNRAS, 401, 1670
Ferland G. J., Korista K. T., Verner D. A., Ferguson J. W., Kingdon J. B., Verner E. M., 1998, PASP, 110, 761
Foreman-Mackey D., Hogg D. W., Lang D., Goodman J., 2013, PASP, 125, 306
Frenk C. S. et al., 1999, ApJ, 525, 554
Fujita Y., Umetsu K., Rasia E., Meneghetti M., Donahue M., Medezinski E., Okabe N., Postman M., 2018a, ApJ, 857, 118
Fujita Y., Umetsu K., Ettori S., Rasia E., Okabe N., Meneghetti M., 2018b, ApJ, 863, 37
Fujita Y. et al., 2019, Galaxies, 7, 8
Geach J. E., Peacock J. A., 2017, Nat. Astron., 1, 795
Ghigna S., Moore B., Governato F., Lake G., Quinn T., Stadel J., 1998, MNRAS, 300, 146
Giocoli C., Meneghetti M., Ettori S., Moscardini L., 2012, MNRAS, 426, 1558
Giocoli C., Meneghetti M., Metcalf R. B., Ettori S., Moscardini L., 2014, MNRAS, 440, 1899
Gruen D. et al., 2013, MNRAS, 432, 1455
Gupta N., Saro A., Mohr J. J., Dolag K., Liu J., 2017, MNRAS, 469, 3069
Heitmann K. et al., 2016, ApJ, 820, 108
Henson M. A., Barnes D. J., Kay S. T., McCarthy I. G., Schaye J., 2017, MNRAS, 465, 3361
Hirschmann M., Dolag K., Saro A., Bachmann L., Borgani S., Burkert A., 2014, MNRAS, 442, 2304
Hoekstra H., Herbonnet R., Muzzin A., Babul A., Mahdavi A., Viola M., Cacciato M., 2015, MNRAS, 449, 685
Hu W., Kravtsov A. V., 2003, ApJ, 584, 702
Klypin A., Yepes G., Gottlöber S., Prada F., Heß S., 2016, MNRAS, 457, 4340

Komatsu E. et al., 2009, ApJS, 180, 330
Komatsu E. et al., 2011, ApJS, 192, 18
Kravtsov A. V., Klypin A. A., Khokhlov A. M., 1997, ApJS, 111, 73
Kwan J., Bhattacharya S., Heitmann K., Habib S., 2013, ApJ, 768, 123
Łokas E. L., Mamon G. A., 2001, MNRAS, 321, 155
Ludlow A. D., Navarro J. F., Li M., Angulo R. E., Boylan-Kolchin M., Bett P. E., 2012, MNRAS, 427, 1322
Ludlow A. D. et al., 2013, MNRAS, 432, 1103
Ludlow A. D., Navarro J. F., Angulo R. E., Boylan-Kolchin M., Springel V., Frenk C., White S. D. M., 2014, MNRAS, 441, 378
Ludlow A. D., Bose S., Angulo R. E., Wang L., Hellwing W. A., Navarro J. F., Cole S., Frenk C. S., 2016, MNRAS, 460, 1214
Macciò A. V., Dutton A. A., van den Bosch F. C., 2008, MNRAS, 391, 1940
Mandelbaum R., Seljak U., Hirata C. M., 2008, J. Cosmol. Astropart. Phys., 8, 006
Mantz A. B., 2019, MNRAS, 485, 4863
Martinsson T. P. K., Verheijen M. A. W., Westfall K. B., Bershady M. A., Andersen D. R., Swaters R. A., 2013, A&A, 557, A131
McClintock T. et al., 2019, MNRAS, 482, 1352
Melchior P., Sheldon E., Drlica-Wagner A., Rykoff E. S., 2015, Astrophysics Source Code Library, record ascl:1511.017
Melchior P. et al., 2017, MNRAS, 469, 4899
Melchior P., Moolekamp F., Jerdee M., Armstrong R., Sun A. L., Bosch J., Lupton R., 2018, Astron. Comput., 24, 129
Meneghetti M. et al., 2014, ApJ, 797, 34
Merten J. et al., 2015, ApJ, 806, 4
Navarro J. F., Frenk C. S., White S. D. M., 1996, ApJ, 462, 563
Navarro J. F., Frenk C. S., White S. D. M., 1997, ApJ, 490, 493
Okabe N., Smith G. P., 2016, MNRAS, 461, 3794
Okoli C., 2017, preprint (arXiv:1711.05277)
Prada F., Klypin A. A., Cuesta A. J., Betancort-Rijo J. E., Primack J., 2012, MNRAS, 423, 3018
Pratt G. W., Pointecouteau E., Arnaud M., van der Burg R. F. J., 2016, A&A, 590, L1
Ragagnin A., Tchipev N., Bader M., Dolag K., Hammer N. J., 2016, Advances in Parallel Computing. IOS Press, Amsterdam, p. 411
Ragagnin A., Dolag K., Moscardini L., Biviano A., D'Onofrio M., 2019, MNRAS, 486, 4001
Raghunathan S. et al., 2019, ApJ, 872, 170
Remus R.-S., Dolag K., 2016, in Sanchez S. F., Morriset C., Delgado-Inglada G., eds, Proceeding of the conference The Interplay between Local and Global Processes in Galaxies. UNAM, Cozumel, Mexico, p. 43,
Remus R.-S., Dolag K., Naab T., Burkert A., Hirschmann M., Hoffmann T. L., Johansson P. H., 2017, MNRAS, 464, 3742
Rey M. P., Pontzen A., Saintonge A., 2018, MNRAS, 485, 1906
Roos M., 2003, Introduction to Cosmology, 3rd edn, Wiley, Hoboken, New Jersey
Rozo E., Bartlett J. G., Evrard A. E., Rykoff E. S., 2014, MNRAS, 438, 78
Saro A. et al., 2014, MNRAS, 440, 2610
Schulze F., Remus R.-S., Dolag K., Burkert A., Emsellem E., van de Ven G., 2018, MNRAS, 480, 4636
Shan H. et al., 2017, ApJ, 840, 104
Shirasaki M., Lau E. T., Nagai D., 2018, MNRAS, 477, 2804
Simet M., McClintock T., Mandelbaum R., Rozo E., Rykoff E., Sheldon E., Wechsler R. H., 2017, MNRAS, 466, 3103
Singh P., Saro A., Costanzi M., Dolag K., 2019, MNRAS, 494, 3728
Springel V., 2005, MNRAS, 364, 1105
Springel V., White S. D. M., Tormen G., Kauffmann G., 2001, MNRAS, 328, 726
Springel V., Di Matteo T., Hernquist L., 2005a, MNRAS, 361, 776
Springel V. et al., 2005b, Nature, 435, 629
Steinborn L. K., Dolag K., Hirschmann M., Prieto M. A., Remus R.-S., 2015, MNRAS, 448, 1504
Steinborn L. K., Dolag K., Comerford J. M., Hirschmann M., Remus R.-S., Teklu A. F., 2016, MNRAS, 458, 1013
Suto Y., 2003, Symposium - International Astronomical Union, Vol. 2016. Cambridge University Press, Cambridge, p. 105
Teklu A. F., Remus R.-S., Dolag K., Beck A. M., Burkert A., Schmidt A. S., Schulze F., Steinborn L. K., 2015, ApJ, 812, 29
Teklu A. F., Remus R.-S., Dolag K., 2016, The Interplay between Local and Global Processes in Galaxies. UNAM, Cozumel , Mexico, p. 41
Tollet E. et al., 2016, MNRAS, 456, 3542
Tornatore L., Borgani S., Dolag K., Matteucci F., 2007, MNRAS, 382, 1050
Umetsu K. et al., 2019, ApJ, 890, 148
van de Sande J. et al., 2019, MNRAS, 484, 869
Wang L., Dutton A. A., Stinson G. S., Macciò A. V., Penzo C., Kang X., Keller B. W., Wadsley J., 2015, MNRAS, 454, 83
Zhang C., Yu Q., Lu Y., 2016, ApJ, 820, 85

APPENDIX A: EFFECTS OF BARYONS

In this appendix section, we show the importance of correctly describing baryon physics on the estimation of halo concentration. Since all simulations (C1–C15) share the same initial conditions, it is possible to study the evolution of the same halo that evolved differently in different cosmologies.

Fig. A1 shows the evolution of both the virial radii and scale radii of haloes in C1 and C1_norad. Fig. A1 (upper panel) shows the stacked ratio of concentration, virial radius, and the scale radius. On an average, C1 haloes have higher concentration parameters ($\approx$ 10–15 per cent higher, up to $\approx$ 20 per cent) and this difference grows with time. Intuitively one may think that the difference in concentration between C1 and C1_norad would be due to a difference in the virial radius. However, the figure shows that it is the scale radius that produce the difference in concentration between the full physics run and the non-radiative one.

Fig. A1 (bottom panel) focuses on the evolution of a single halo (bottom left panel shows the evolution of the halo in C1, whereas the bottom right panel shows the same halo in C1_norad). Simulations without radiative cooling produce haloes with lower concentration with respect to their full physics counterpart (i.e. $c_{\rm vir} \approx 6$ lowers down to $c_{\rm vir} \approx 5$). This example shows that in non-radiative simulations, concentration decreases even if the full physics counterpart is characterized by the same accretion history ('jumps' in concentration and $r_{\rm s}$ values happen at the same scale factor).

Dynamical state is known to be related to halo concentrations (Ludlow et al. 2012) and can be quantified using the virial ratio (Cui et al. 2017), $(2T - E_{\rm s})/W$, where W is the total potential energy, T is the total kinetic energy (including gas thermal pressure), and $E_{\rm s}$ is the energy from surface pressure P (from kinetic and thermal energy) at the halo boundary. As described in Chandrasekhar (1961), $E_{\rm s}$ is given by

$$E_{\rm s} = \oint P(\mathbf{r})\mathbf{r} \cdot \mathrm{d}\mathbf{S}. \tag{A1}$$

Cui et al. (2017) showed that baryonic physics can lower the virial ratio up to 10 per cent w.r.t. DMO runs and Zhang, Yu & Lu (2016) showed that merger time-scale is shortened by a factor of up to 3 for merging clusters with gas fractions 0.15, compared to the time-scale obtained with no gas.

Fig. A2 shows $E_{\rm s}/W$ *versus* K/W for a DMO run (left-hand panel) and a hydrodynamic run (right-hand panel) that shares the same initial conditions.[6] The two runs display a different behaviour for

[6]We use Magneticum/Box0_mr simulation, with 2.7 Gpc h^{-1} size and gravitational softening down to 2.6×10^9 kpc h^{-1}, gas and DM mass particles of 2.610^9 and 2.610^{10} $\mathrm{M}_\odot\, h^{-1}$, respectively, as presented in Bocquet et al. (2016).

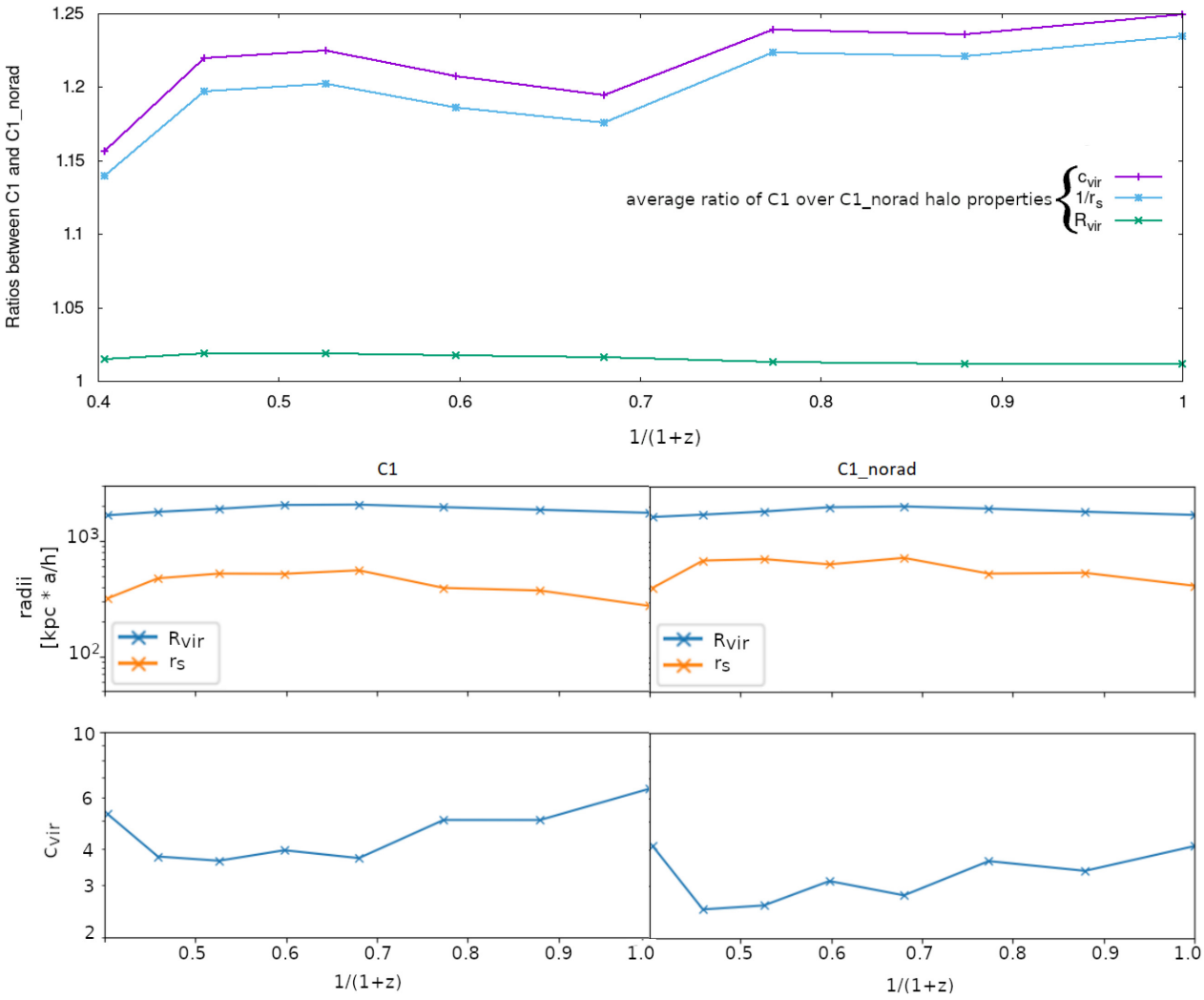

Figure A1. Evolution of virial and scale radii and concentration of haloes in simulations C1 and C1_norad. Upper panel shows the stacked average over 50 haloes of ratios of $c_{\rm vir}$ (magenta top line), $1/r_{\rm s}$ (cyan middle line), and $R_{\rm vir}$ (bottom green line) between C1 and C1_norad. Lower panel shows the evolution $R_{\rm vir}$ (blue top line) and $r_{\rm s}$ (orange bottom line) and $c_{\rm vir}$ in blue, of the same halo in the simulation C1 (bottom left panels) and C1_norad (bottom right panels).

highly concentrated objects ($c > 4$): DMO ones have low surface pressure and low total kinetic energy, while hydrodynamic ones show a much more complex and noisy relation between $E_{\rm s}$, W, and c_{200c}.

It is well known that concentration does depend on dynamical state. Here, we also noted how hydrodynamic simulations compared to DMO runs do show even a more noisy and complex relation between concentration and the virial ratio. However, given that the majority of observational studies that investigate large cluster samples lack data to accurately determine their dynamical state (see e.g. studies presented in Hoekstra et al. 2015; Okabe & Smith 2016; Melchior et al. 2018; Bocquet et al. 2019; Dietrich et al. 2019; Mantz 2019, and references therein), they will benefit from an Mc relation built from hydrodynamic simulations that already averages over all possible dynamical states of a halo, as in this work.

The average concentration of haloes shown in Fig. 2 are lower than the concentration computed using the dark matter density profile presented in a previous work on Magneticum simulations (Ragagnin et al. 2019, which uses the same cosmology as C8). The median concentration for cosmology C8 is $c_{200c} \approx 3.5$ for the total matter profile, while the dark matter concentration presented in Ragagnin et al. (2019) has $c_{200c} \approx 4.3$.

Such discrepancy is due to the fact that dark matter component is more peaked in the central region with respect to the total matter density. Fig. A3 shows an example of the matter density profiles of a Magneticum halo. Here, the DM halo has a scale radius of 139 kpc h^{-1} while the total matter scale radius is 154 kpc h^{-1}: collisional particles and stars formed from them (and their associated heating processes as SN and AGN feedback) are capable of lowering a concentration parameter of $\approx$ 20 per cent.

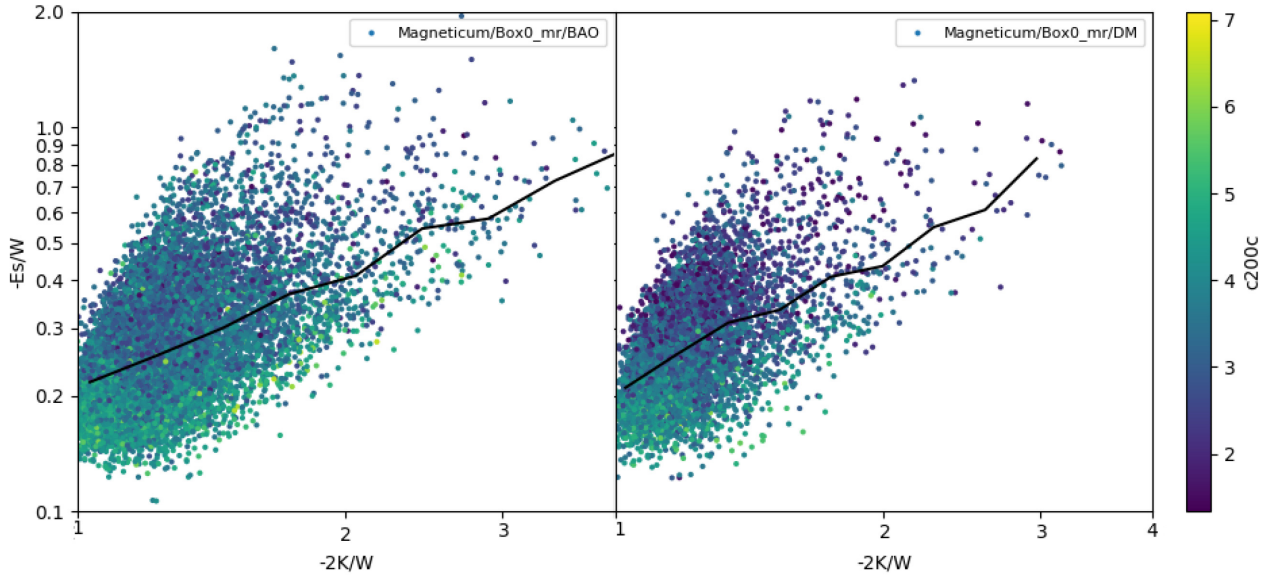

Figure A2. Kinetic term *K versus* energy from the surface pressure E_s scaled by total potential energy W for the same initial condition evolved with baryon physics (left-hand panel) and a DMO run (right-hand panel). Black solid lines show the median E_s/W.

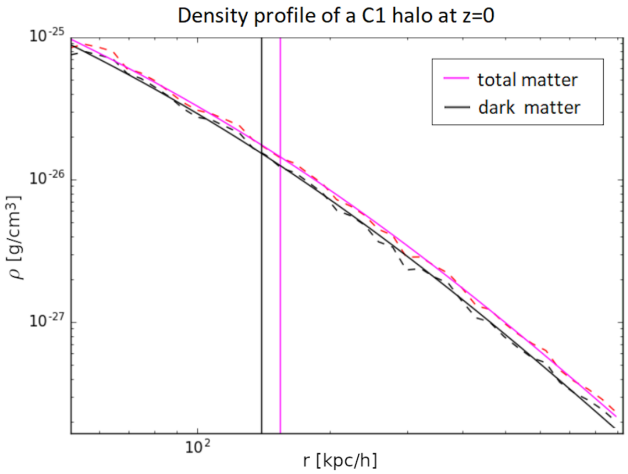

Figure A3. Density profile of both dark matter (dashed black) and total matter (dashed pink) up to the virial radius $R_{\rm vir} = 930\,{\rm kpc}\,h^{-1}$ and the corresponding NFW profile (solid lines) for a halo of C1 simulation at $z = 0$. Vertical lines correspond, respectively, to the dark matter profile scale radius ($139\,{\rm kpc}\,h^{-1}$) and the total matter profile has a scale radius $r_s = 154\,{\rm kpc}\,h^{-1}$.

APPENDIX B: COSMOLOGY–MASS–REDSHIFT–CONCENTRATION RELATION LITE

Given the weak dependence of mass from the concentration (at least in the mass range of interests of cluster of galaxies), we provide a cosmology–redshift–mass–concentration fit, where in equation (5) we parametrize the dependence of the cosmology only in the normalization and in the redshift dependence as the following:

$$\begin{aligned} A &= A_0 + \alpha_{\rm m}\ln\left(\frac{\Omega_{\rm m}}{\Omega_{\rm m,p}}\right) + \alpha_{\rm b}\ln\left(\frac{\Omega_{\rm b}}{\Omega_{\rm b,p}}\right) + \\ &\quad + \alpha_\sigma \ln\left(\frac{\sigma_8}{\sigma_{8,\rm p}}\right) + \alpha_{\rm h}\ln\left(\frac{h_0}{h_{0,\rm p}}\right) \\ B &= B_0 \\ C &= C_0 + \gamma_{\rm m}\ln\left(\frac{\Omega_{\rm m}}{\Omega_{\rm m,p}}\right) + \gamma_{\rm b}\ln\left(\frac{\Omega_{\rm b}}{\Omega_{\rm b,p}}\right) + \\ &\quad + \gamma_\sigma \ln\left(\frac{\sigma_8}{\sigma_{8,\rm p}}\right) + \gamma_{\rm h}\ln\left(\frac{h_0}{h_{0,\rm p}}\right). \end{aligned} \tag{B1}$$

Table B1 shows the results of this fit, with the same procedure as in Section 4, where pivot values are the ones for the reference cosmology C8 and errors are assigned by performing the same fit as in Singh et al. (2019).

Table B2 shows the results of the Mc plane where we fit the NFW profile of the dark matter density profile only. The functional form is as in equation (B1), with the same procedure as the previous one (thus, as in Section 4).

Table B1. Pivots and fit parameters for the cosmology dependent aMc plane as Table 2, here the logarithmic slope of mass is not dependent on cosmology, thus we fit equations (5) and (B1), for concentration overdensities of $\Delta = \Delta_{\mathtt{vir}}$, Δ_{200c}, Δ_{500c}, Δ_{2500c}, and Δ_{200m}. The pivots $\Omega_{\mathrm{m,p}}$, $\Omega_{\mathrm{b,p}}$, σ_8, and h_0 in equation (7) are the cosmological parameters of C8 as in Table 1 ($\Omega_{\mathrm{m}} = 0.272$, $\Omega_{\mathrm{b}} = 0.0456$, $\sigma_8 = 0.809$, $h_0 = 0.704$). Errors on A_0, B_0, C_0, and σ are omitted as they are all < 0.001 per cent. The package HYDRO_MC contains a script that utilizes this relation (#1).

Parameter	Overdensity				
	vir	200c	500c	2500c	200m
M_{p} ($M_\odot$)	$1.99e+14$	$1.74e+14$	$1.37e+14$	$6.87e+13$	$2.24e+14$
a_{p}	0.877	0.877	0.877	0.877	0.877
A_0	1.499	1.238	0.859	0.122	1.688
B_0	−0.048	−0.053	−0.060	−0.037	−0.044
C_0	0.520	0.201	0.187	0.110	0.910
α_{m}	0.423 ± 0.006	0.60 ± 0.01	0.63 ± 0.01	0.7273 ± 0.0006	0.201 ± 0.003
α_{b}	-0.141 ± 0.006	-0.152 ± 0.006	-0.131 ± 0.005	-0.179 ± 0.004	-0.186 ± 0.006
α_σ	0.65 ± 0.02	0.65 ± 0.02	0.61 ± 0.03	0.516 ± 0.003	0.60 ± 0.02
α_{h}	-0.28 ± 0.01	-0.25 ± 0.02	-0.27 ± 0.02	-0.23 ± 0.01	-0.17 ± 0.02
γ_{m}	0.19 ± 0.01	0.360 ± 0.010	0.336 ± 0.009	0.36 ± 0.01	-0.10 ± 0.01
γ_{b}	0.02 ± 0.06	-0.15 ± 0.06	-0.04 ± 0.05	0.00 ± 0.07	0.00 ± 0.06
γ_σ	0.76 ± 0.05	0.72 ± 0.04	0.89 ± 0.04	0.94 ± 0.06	0.61 ± 0.05
γ_{h}	-0.4 ± 0.2	-0.1 ± 0.2	-0.4 ± 0.2	-0.5 ± 0.2	-0.4 ± 0.2
σ	0.388031	0.384516	0.376690	0.382868	0.388477

Table B2. Fit parameters for the cosmology-dependent aMc plane as Table 2, here we computed the concentration using the scale radius of the dark matter density profile, plus the logarithmic slope of mass is not dependent on cosmology. We fit equations (5) and (B1), for concentration overdensities of $\Delta = \Delta_{\mathrm{vir}}$, Δ_{200c}, Δ_{500c}, Δ_{2500c}, and Δ_{200m}. The pivots $\Omega_{\mathrm{m,p}}$, $\Omega_{\mathrm{b,p}}$, σ_8, and h_0 in equation (7) are the cosmological parameters of C8 as in Table 1 ($\Omega_{\mathrm{m}} = 0.272$, $\Omega_{\mathrm{b}} = 0.0456$, $\sigma_8 = 0.809$, $h_0 = 0.704$). Errors on A_0, B_0, C_0, and σ are omitted as they are all < 0.001 per cent. The package HYDRO_MC contains a script that utilizes this relation (#1).

Parameter	Overdensity				
	vir	200c	500c	2500c	200m
A_0	1.499	1.238	0.979	0.213	1.798
B_0	−0.048	−0.053	−0.039	−0.015	−0.034
C_0	0.520	0.201	0.178	0.055	0.918
α_{m}	0.42 ± 0.05	0.60 ± 0.01	0.46 ± 0.07	0.588 ± 0.001	0.008 ± 0.007
α_{b}	-0.14 ± 0.03	-0.152 ± 0.006	-0.08 ± 0.03	-0.204 ± 0.010	-0.072 ± 0.006
α_σ	0.65 ± 0.03	0.65 ± 0.02	0.47 ± 0.05	0.363 ± 0.006	0.53 ± 0.01
α_{h}	-0.28 ± 0.05	-0.25 ± 0.02	-0.33 ± 0.05	-0.47 ± 0.03	0.03 ± 0.01
γ_{m}	0.19 ± 0.04	0.360 ± 0.010	0.34 ± 0.01	0.51 ± 0.03	-0.23 ± 0.01
γ_{b}	0.02 ± 0.06	-0.15 ± 0.06	-0.4 ± 0.1	-0.7 ± 0.1	-0.09 ± 0.06
γ_σ	0.76 ± 0.06	0.72 ± 0.04	0.5 ± 0.1	0.3 ± 0.1	0.45 ± 0.02
γ_{h}	-0.4 ± 0.2	-0.1 ± 0.2	-1.1 ± 0.4	-1.9 ± 0.5	0.02 ± 0.06
σ	0.39	0.384516	0.51	0.484290	0.498887

APPENDIX C: THEORETICAL SCATTER OF MASS CONVERSION USING AN MC RELATION

Equation system (11) shows how the concentration in an overdensity Δ_2 is uniquely identified by the concentration in Δ_1 by solving bottom equation in equation (11). Although there are four variables in equation (11) (namely $M_{\Delta 1}$, $M_{\Delta 2}$, $c_{\Delta 1}$, and $c_{\Delta 2}$), since there are two equations the system depends on two of them.

Hu & Kravtsov (2003) provide a fitting formula for $c_{\Delta 2}$ as a function of $c_{\Delta 1}$. On the other hand, since $c_{\Delta 2}$ depends monotonically from right-hand side of equation (11), in this work we convert the values from $c_{\Delta 1}$ to $c_{\Delta 2}$ using the fixed-point technique derived by solving equation (11) the Banach–Cacioppoli theorem (see e.g. Ciesielski 2007, for a review).

To evaluate $c_{\Delta 2}$, we start with a guess value of $c_{\Delta 1}$ and iteratively apply it to equation (11) in order to get the new value of value of $c_{\Delta 2}$, until it converges, practically we fix $\frac{\Delta_1}{\Delta_2}$ and $c_{\Delta,1}$ rewrite equation (11) as

$$\tilde{c}(x) \equiv c_{\Delta 1} \cdot \left(\frac{\Delta_1}{\Delta_2} \frac{f(x)}{f(c_{\Delta 1})} \right)^{\frac{1}{3}}$$
$$c_{\Delta 2} = \tilde{c}(c_{\Delta 2}). \qquad \text{(C1)}$$

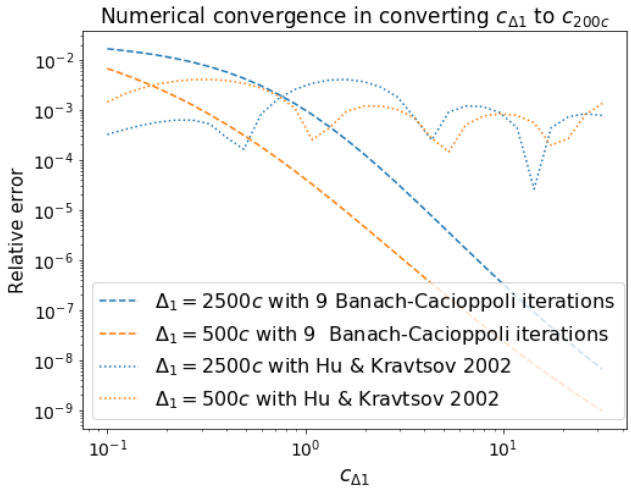

Figure C1. Relative error when converting the concentration using equation (C1; i.e. Banach–Cacioppoli theorem) or using the method proposed in Hu & Kravtsov (2003).

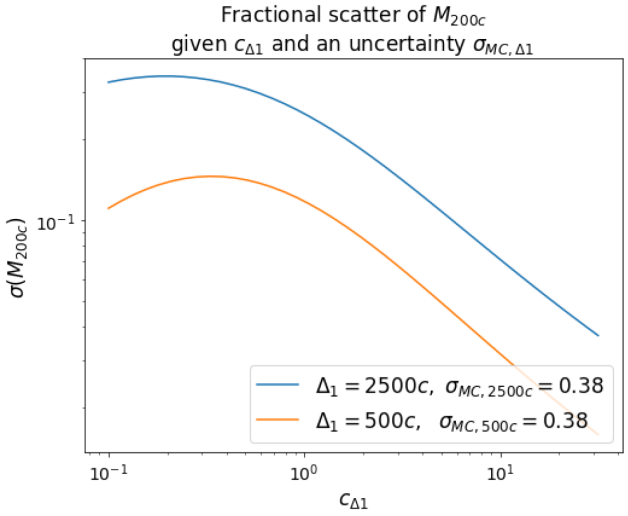

Figure C2. Analytical uncertainty on the concentration obtained by the theoretical propagation of error.

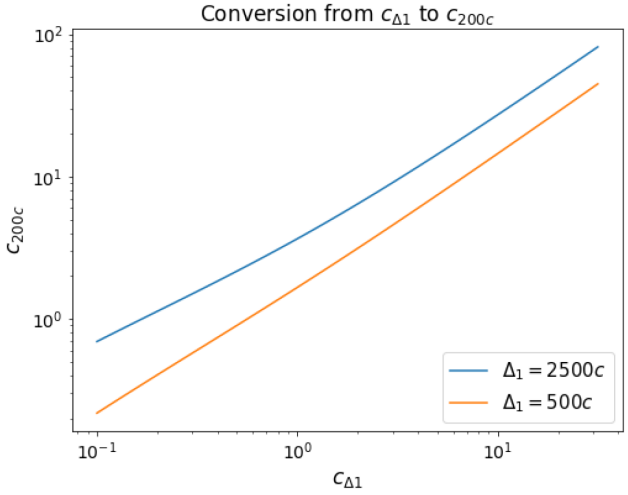

Figure C3. Analytical value of c_{200c} for a given concentration $c_{\Delta 1}$. We used $\Delta 1 = 500c$ and $\Delta 1 = 2500c$.

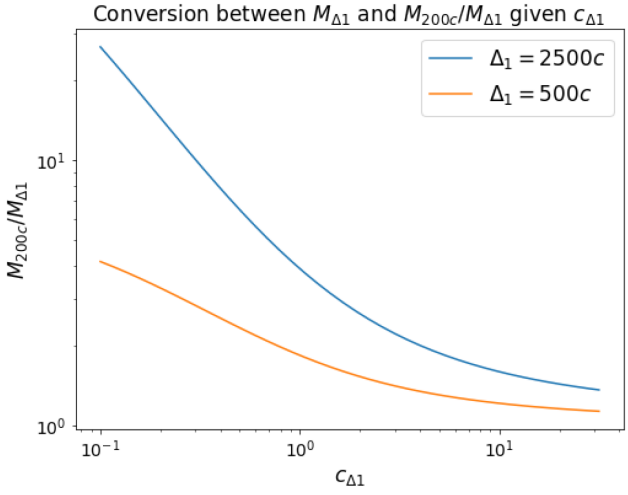

Figure C4. Analytical value of M_{200c} with respect to $M_{\Delta 1}$ for a given concentration $c_{\Delta 1}$. We used $\Delta 1 = 500c$ and $\Delta 1 = 2500c$.

We found that the relative error after nine iterations is, at the worst, comparable with Hu & Kravtsov (2003) and can go down to 10^{-9} for concentration values higher than 20. As a first value, we choose $c_{\Delta 1}$, so

$$c_{\Delta 2} \approx \tilde{c}\,(\tilde{c}\,(\tilde{c}\,(\tilde{c}\,(\tilde{c}\,(\tilde{c}\,(\tilde{c}\,(\tilde{c}\,(c_{\Delta 1})))))))) \,. \tag{C2}$$

Fig. C1 shows the relative error when converting M_{500c} and M_{2500c} to M_{200c}. Both approach have an error smaller than ≈ 0.1 per cent, while the iteration proposed here can reach much more precise value and it is easier to implement. Only nine iterations produce a relative error that in the worst case is comparable with technique in Hu & Kravtsov (2003) and it is capable of going down to 10^{-8}.

Fig. C2 shows the conversion from overdensities $\Delta_2 = 2500$ and $\Delta_2 = 500$ to $\Delta_1 = 200$. These relations are nearly linear with a deviation for lower concentrations.

Another interesting property of equation (11) is the possibility of knowing $M_{\Delta 2}/M_{\Delta 1}$ only by knowing $c_{\Delta 1}$.

Fig. C3 shows such conversions for overdensities Δ_{2500c} and Δ_{500c} to $\Delta_{200c}1$. This conversion gets flatter and flatter as the concentration increases, implying that the higher the concentration the lower the error one makes in this conversion.

It is possible to estimate this uncertainty analytically. Given the fact that Mc relations are known with uncertainties, it is interesting to see how to propagate the error analytically when converting from $c_{\Delta 1}$ to $c_{\Delta 2}$, which is proportional to the derivative coming from equation (9):

$$\frac{\mathrm{d}c_{\Delta 2}}{\mathrm{d}c_{\Delta 1}} = \frac{c_{\Delta 2}}{c_{\Delta 1}} + \frac{1}{3}\frac{c_{\Delta 2}}{f\,(c_{\Delta 1})}\frac{\mathrm{d}f(c)}{\mathrm{d}c}\bigg|_{c=c_{\Delta 1}}\frac{\mathrm{d}c_{\Delta 2}}{\mathrm{d}c_{\Delta 1}} - \\ -\frac{1}{3}\frac{c_{\Delta 2}}{f\,(c_{\Delta 1})}\frac{\mathrm{d}f(c)}{\mathrm{d}c}\bigg|_{c=c_{\Delta 2}}, \tag{C3}$$

where $f(c)$ is, in case of imposing an NFW profile, given in equation (10). One can rearrange equation (C3) to isolate the derivative:

$$\frac{\mathrm{d}c_{\Delta 2}}{\mathrm{d}c_{\Delta 1}} = \frac{\dfrac{c_{\Delta 2}}{c_{\Delta 1}} - \dfrac{1}{3}\dfrac{c_{\Delta 2}}{f\,(c_{\Delta 1})}\dfrac{\mathrm{d}f(c)}{\mathrm{d}c}\bigg|_{c=c\Delta 2}}{1 - \dfrac{1}{3}\dfrac{c_{\Delta 2}}{f\,(c_{\Delta 1})}\dfrac{\mathrm{d}f(c)}{\mathrm{d}c}\bigg|_{c=c\Delta 1}}. \tag{C4}$$

One can understand how a uncertainty propagates analytically from $M_{\Delta 2}(M_{\Delta 1}, c_{\Delta 1})$ in equation (11), by computing the derivative

$$\frac{\mathrm{d}M_{\Delta 2}}{\mathrm{d}c_{\Delta 1}} = \frac{\partial M_{\Delta 2}}{\partial c_{\Delta 1}} + \frac{\partial M_{\Delta 2}}{\partial M_{\Delta 1}}\frac{\mathrm{d}M_{\Delta 1}}{\mathrm{d}c_{\Delta 1}},$$

given the very weak dependence of mass from concentration, we can approximate

$$\frac{\mathrm{d}M_{\Delta 1}}{\mathrm{d}c_{\Delta 1}} \approx 0,$$

one gets

$$\frac{\mathrm{d}M_{\Delta 2}}{\mathrm{d}c_{\Delta 1}} = 3M_{\Delta 2}\left(\frac{1}{c_{\Delta 2}}\frac{\mathrm{d}c_{\Delta 2}}{\mathrm{d}c_{\Delta 1}} - \frac{1}{c_{\Delta 1}}\right),$$

where $\mathrm{d}c_{\Delta 2}/\mathrm{d}c_{\Delta 1}$ is evaluated as in equation (C4).

Fig. C4 shows the uncertainty variation when converting to M_{200} for a scatter in the concentration compatible with the scatter we found in our Mc relation (see Table 2). This is helpful in understanding the actual scatter one finds in real case scenarios as in Sections 5.1 and 5.2.

This paper has been typeset from a TEX/LATEX file prepared by the author.